# Evolving viscous anisotropy in the upper mantle and its geodynamic implications

Agnes Kiraly[1,1], Clinton P. Conrad[2,2], and Lars Hansen[3,3]

[1]Centre for Earth Evolution and Dynamics (CEED), University of Oslo
[2]Centre for Earth Evolution and Dynamics
[3]University of Minnesota-Twin Cities

November 30, 2022

## Abstract

Asthenospheric shear causes some minerals, particularly olivine, to develop anisotropic textures that can be detected seismically. In laboratory experiments, these textures are also associated with anisotropic viscous behavior, which should be important for geodynamic processes. To examine the role of anisotropic viscosity for asthenospheric deformation, we developed a numerical model of coupled anisotropic texture development and anisotropic viscosity, both calibrated with laboratory measurements of olivine aggregates. This model characterizes the time-dependent coupling between large-scale formation of lattice-preferred orientation (i.e., texture) and changes in asthenospheric viscosity for a series of simple deformation paths that represent upper-mantle geodynamic processes. We find that texture development beneath a moving surface plate tends to align the a-axes of olivine into the plate-motion direction, which weakens the effective viscosity in this direction and increases plate velocity for a given driving force. Our models indicate that the effective viscosity increases for shear in the horizontal direction perpendicular to the a-axes. This increase should slow plate motions and new texture development in this perpendicular direction, and could impede changes to the plate motion direction for 10s of Myrs. However, the same well-developed asthenospheric texture may foster subduction initiation perpendicular to the plate motion and deformations related to transform faults, as shearing on vertical planes seems to be favored across a sub-lithospheric olivine texture. These end-member cases examining shear-deformation in the presence of a well-formed asthenospheric texture illustrate the importance of the mean olivine orientation, and its associated viscous anisotropy, for a variety of geodynamic processes.

## Hosted file

`data_archive_kiralyetal2020_anisotropicviscosity.docx` available at [https://authorea.com/users/558502/articles/607659-evolving-viscous-anisotropy-in-the-upper-mantle-and-its-geodynamic-implications](https://authorea.com/users/558502/articles/607659-evolving-viscous-anisotropy-in-the-upper-mantle-and-its-geodynamic-implications)

# Evolving viscous anisotropy in the upper mantle and its geodynamic implications

Á. Király[1], C.P. Conrad[1], L.N. Hansen[2]

[1] Centre for Earth Evolution and Dynamics, University of Oslo, Norway

[2] Department of Earth and Environmental Sciences, University of Minnesota, Minneapolis, MN, USA

## Key Points

- We develop models of olivine texture evolution within deforming asthenosphere, and the associated directional variations in viscosity
- The effective viscosity of textured olivine can vary by an order of magnitude, depending on which slip system dominates the deformation.
- Anisotropic viscosity promotes faster plate motion & ridge-parallel subduction initiation, but impedes directional changes in plate motion

## Key words

Olivine, Anisotropic viscosity, LPO, Texture development, Plate motions, Asthenospheric deformation

20  *Abstract*

21  Asthenospheric shear causes some minerals, particularly olivine, to develop anisotropic

22  textures that can be detected seismically. In laboratory experiments, these textures are also

23  associated with anisotropic viscous behavior, which should be important for geodynamic

24  processes. To examine the role of anisotropic viscosity for asthenospheric deformation, we

25  developed a numerical model of coupled anisotropic texture development and anisotropic

26  viscosity, both calibrated with laboratory measurements of olivine aggregates. This model

27  characterizes the time-dependent coupling between large-scale formation of lattice-preferred

28  orientation (i.e., texture) and changes in asthenospheric viscosity for a series of simple

29  deformation paths that represent upper-mantle geodynamic processes. We find that texture

30  development beneath a moving surface plate tends to align the a-axes of olivine into the plate-

31  motion direction, which weakens the effective viscosity in this direction and increases plate

32  velocity for a given driving force. Our models indicate that the effective viscosity increases

33  for shear in the horizontal direction perpendicular to the a-axes. This increase should slow

34  plate motions and new texture development in this perpendicular direction, and could impede

35  changes to the plate motion direction for 10s of Myrs. However, the same well-developed

36  asthenospheric texture may foster subduction initiation perpendicular to the plate motion and

37  deformations related to transform faults, as shearing on vertical planes seems to be favored

38  across a sub-lithospheric olivine texture. These end-member cases examining shear-

39  deformation in the presence of a well-formed asthenospheric texture illustrate the importance

40  of the mean olivine orientation, and its associated viscous anisotropy, for a variety of

41  geodynamic processes.

42

## *Plain language summary*

The uppermost layer of Earth's mantle, the asthenosphere, experiences large deformations due to a variety of tectonic processes. During deformation, grains of olivine, the main rock-forming mineral in the asthenosphere, rotate into a preferred direction parallel to the deformation, developing a texture that can affect the response of the asthenosphere to tectonic stresses. Laboratory measurements show that the deformation rate depends on the orientation of the shear stress relative to the olivine texture. We use numerical models to apply the findings of the laboratory measurements to geodynamic situations that are difficult to simulate in a laboratory. These models track the development of olivine texture and its directional response to shear stress, which are highly coupled. Our results suggest that anisotropic viscosity in the asthenosphere can significantly affect the motions of tectonic plates, as plate motion in a continuous direction should become faster while abrupt changes in the direction of plate motion should meet high resistance in the underlying asthenosphere. We suggest that olivine textures in the asthenosphere play a critical role in upper mantle dynamics.

## 1. Introduction

The physical characteristics of the upper mantle, e.g. its density and rheology, control a variety of surface features, such as general tectonic regime, faulting characteristics, dynamic topography, and plate velocity. Many of these features are thus related to the properties of olivine, which comprises ~60% of the upper mantle (Stixrude and Lithgow-Bertelloni, 2005). It has long been known that olivine is anisotropic in its elastic properties, and this directional dependence has been observed in the upper mantle using seismic waves (e.g., Tanimoto and Anderson, 1984). This observed seismic anisotropy is mainly the result of the lattice preferred orientation (LPO, or texture) of the olivine crystals, which causes the speed of seismic waves to depend on propagation direction and additionally causes shear waves to split into two perpendicularly polarized waves (faster and slower) (Bamford and Crampin, 1977; Christensen, 1984; Mainprice et al., 2015). The texture (or LPO) itself is thought to result from shear strain in the upper mantle, which causes olivine crystals to rotate into a preferred direction, generally with the seismically fast axis parallel to the direction of shearing (e.g., Ribe, 1989; Karato and Wu, 1993). Seismic observations of this anisotropy have been used to infer patterns of upper-mantle deformation (Long and Becker, 2010), for example related to tectonic plate motions (e.g., Becker, 2008; Becker et al., 2014, 2008, 2003; Behn et al., 2004; Conrad and Behn, 2010; Gaboret et al., 2003), subduction (e.g., Long, 2013), continental collision (e.g., Silver, 1996), and motion on transform faults (e.g., Eakin et al., 2018).

Early laboratory experiments found that olivine is not limited to anisotropy in its elastic properties, but also exhibits anisotropy in its viscosity. Durham and Goetze (1977) demonstrated that the deformation rate of a single olivine crystal is orientation dependent and can vary by a factor of 50. To assess the role of single-crystal anisotropy in controlling the anisotropy of an aggregate of crystals, Hansen et al. (2012) first deformed aggregates of olivine in torsion and subsequently deformed them in extension. In torsion, the samples gradually weaken as the texture forms, but subsequent extensional deformation normal to the initial shear plane is characterized by a factor of 14 increase in viscosity. Similarly, but in a reverse order, Hansen et al., (2016b) first deformed aggregates of olivine in extension and subsequently deformed them in torsion. In extension, the samples gradually weaken as the texture forms, but subsequent torsional deformation is again characterized by much higher viscosities. Taken together, these experiments demonstrate that prolonged deformation in a consistent orientation leads to texture formation that reduces the viscosity, and a subsequent change in the orientation of deformation results in a dramatic increase in the viscosity.

91     However, Hansen et al.'s (2016b) laboratory experiments were only able to test a small

92     number of deformation paths (i.e., first extension, then torsion, and *vice versa*), making it

93     difficult to directly apply their results to deformation in the mantle. To apply their results

94     more generally to mantle deformation, Hansen et al., (2016a) used the existing experiments to

95     define and calibrate a mechanical model of slip-system activities and texture development

96     within olivine aggregates. This model can predict both the evolution of olivine textures and

97     the associated anisotropic viscous behavior for olivine aggregates undergoing arbitrary

98     deformation paths. This coupled micromechanical and textural development model enables us

99     to investigate the role of viscous anisotropy for a range of geodynamic processes.

100    Decades ago, researchers used early numerical modeling techniques to test the relevance of

101    viscous anisotropy on geodynamical processes, such as mantle convection or post-glacial

102    rebound (Christensen, 1987). These studies relied on the laboratory measurements of Durham

103    and Goetze (1977), which constrained the anisotropic behavior of single olivine crystals, and

104    the work of Karato (1987), who studied the mechanisms of olivine texture formation. Due to

105    the absence of more detailed laboratory data, previous modelers assumed transverse isotropy

106    in a two-dimensional mantle (i.e., isotropic viscosity for shearing in the horizontal plane, and

107    anisotropy expressed as differences between shearing in the horizontal and vertical

108    directions). More recently, the effect of anisotropic viscosity on mantle convection has been

109    revisited (Mühlhaus et al., 2003), with additional investigations into Raleigh-Taylor

110    instabilities and subduction-zone processes within an anisotropically viscous mantle and/or

111    lithosphere (Lev and Hager, 2011, 2008). These studies are based on the director method

112    (Mühlhaus et al., 2002), which models olivine orientations as a set of directors, that is, 2D

113    unit vectors pointing normal to the easy shear plane. Anisotropic viscosity is expressed by a

114    combination of normal and shear viscosities, and the effective shear viscosity is a function of

115    the distribution of the directors. Furthermore, because the directors are advected and rotated

116    by the flow, this method effectively couples texture development to the anisotropic viscosity

117    of the mantle. The 2D nature of the director method, however, limits its ability to capture the

118    complete anisotropy associated with olivine, which has three independent slip systems that

119    accommodate deformation at different rates (Hansen et al., 2016a).

120    Here we have modified the director method to accommodate three-dimensional deformations

121    of olivine aggregates using the micromechanical approach of Hansen et al. (2016a). This

122    model is calibrated by laboratory constraints on slip system activities and parameters of

123    texture development (i.e., the relative rotation rates of the different olivine slip systems, see

124   Table 1 in Hansen et al, 2016a). The resulting model allows us to explore both the texture
125   development of an olivine aggregate in a wide range of deformation paths and the mechanical
126   response of these textured aggregates to applied stresses associated with these deformation
127   paths. Our goal is to create first-order models of tectonic plate movement subject to a
128   continuous driving force (e.g., slab pull) in one direction. As the olivine texture develops in
129   the asthenosphere, we expect the mechanical response of the system to change as a function
130   of time and accumulated strain, resulting in a changing plate velocity. Next, by changing the
131   direction of the driving force, we can examine the response of the system to the application of
132   stress in a new direction. The resulting deformation paths are analogs for geodynamic
133   applications such as changes in the direction of plate movement, lithospheric dripping,
134   initiation of subduction, and transform faulting. These simple exercises lead us to a better
135   understanding of the interplay among olivine-texture development, anisotropic mantle
136   rheology, and large-scale geodynamic processes.

137   ## 2.  Methods

138   ### 2.1 Mathematical formulation

139   Our method is based on the micromechanical model described and characterized by Hansen et
140   al. (2016a). This approach uses a pseudo-Taylor approximation (after Taylor, 1938) to
141   calculate the stress needed to create an equivalent strain rate on each olivine crystal, allowing
142   for slip along three linearly independent slip systems. Each slip system is characterized by a
143   critical shear stress that describes its strength relative to the isotropic strength of the
144   aggregate. The best-fit model parameters obtained by Hansen et al. (2016a) for the pseudo-
145   Taylor model are the following: 0.30 for the (010)[100] slip system, 0.27 for the (001)[100]
146   slip system, and 1.29 for the (010)[001] slip system. The micromechanical model is coupled
147   to a texture development model, in which the deformation of the olivine aggregate results in
148   grain rotations. The rotation rate depends on the orientation of each grain with respect to the
149   deformation, and a set of texture parameters that define the relative rotation rates along the
150   four olivine slip systems (see Table 1 in Hansen et al., 2016a). These combined models
151   provide the basis for a method to calculate the anisotropic viscosity (or conversely, the
152   fluidity) for any given olivine texture. The resulting three-dimensional tensor can then be used
153   to predict the deformation behavior for several geodynamic applications. In the following, we
154   present details of this method and the results of first-order models in which the olivine-rich

155  upper mantle undergoes different deformation paths induced by temporal variations in an
156  applied shear stress.

157  To calculate the strain rate induced by the imposed stress, some further steps are necessary
158  beyond those described by the mechanical model of Hansen et al. (2016a). The macroscopic
159  constitutive relationship between stress and strain rate for an anisotropic viscous medium is

160  $$\sigma_{kl} = \eta_{ijkl}\dot{\varepsilon}_{ij} \,,$$  (1)

161  where $\dot{\varepsilon}_{ij} = \frac{1}{2}\left(\frac{\partial v_i}{\partial x_j} + \frac{\partial v_j}{\partial x_i}\right)$ is the strain-rate tensor, $\sigma_{kl}$ is the deviatoric-stress tensor, and $\eta_{ijkl}$
162  is the viscosity tensor (Christensen, 1987; Pouilloux et al., 2007). Due to their symmetry, the
163  deviatoric-stress and the strain-rate tensors can both be reduced to vectors using Kelvin
164  notation, which preserves the norm of each of the tensors in (1) (Dellinger et al., 1998),

165
$$\dot{\varepsilon}_{ij} = \begin{bmatrix} \dot{\varepsilon}_{11} & \dot{\varepsilon}_{12} & \dot{\varepsilon}_{13} \\ \dot{\varepsilon}_{12} & \dot{\varepsilon}_{22} & \dot{\varepsilon}_{23} \\ \dot{\varepsilon}_{13} & \dot{\varepsilon}_{23} & \dot{\varepsilon}_{33} \end{bmatrix} \equiv \begin{bmatrix} \dot{\varepsilon}_{11} \\ \dot{\varepsilon}_{22} \\ \dot{\varepsilon}_{33} \\ \sqrt{2}\dot{\varepsilon}_{23} \\ \sqrt{2}\dot{\varepsilon}_{13} \\ \sqrt{2}\dot{\varepsilon}_{12} \end{bmatrix} \equiv \begin{bmatrix} \dot{\varepsilon}_1 \\ \dot{\varepsilon}_2 \\ \dot{\varepsilon}_3 \\ \dot{\varepsilon}_4 \\ \dot{\varepsilon}_5 \\ \dot{\varepsilon}_6 \end{bmatrix}$$  (2)

166

167
$$\sigma_{ij} = \begin{bmatrix} \sigma_{11} & \sigma_{12} & \sigma_{13} \\ \sigma_{12} & \sigma_{22} & \sigma_{23} \\ \sigma_{13} & \sigma_{23} & \sigma_{33} \end{bmatrix} \equiv \begin{bmatrix} \sigma_{11} \\ \sigma_{22} \\ \sigma_{33} \\ \sqrt{2}\sigma_{23} \\ \sqrt{2}\sigma_{13} \\ \sqrt{2}\sigma_{12} \end{bmatrix} \equiv \begin{bmatrix} \sigma_1 \\ \sigma_2 \\ \sigma_3 \\ \sigma_4 \\ \sigma_5 \\ \sigma_6 \end{bmatrix}.$$  (3)

168  It follows that the viscosity can be reduced to a 6x6 tensor (e.g., Pouilloux et al., 2007).
169  Because of the non-linear rheological behavior of olivine, the viscosity tensor is also a
170  function of stress. The rheology can thus be expressed by a stress-independent material
171  constant ($\underline{A}$), which relates to the viscosity as

172  $$inv\left(\eta_{ij}\right) = A_{ij} \cdot II_\sigma^{(n-1)/2} \,.$$  (4)

173  Equation 4 describes the fluidity of the material at a given stress, where $II_\sigma$ denotes the
174  second invariant of the deviatoric stress and $n$ is the power-law factor. Using eq. (4), the strain
175  rate can be expressed as a function of the stress and the fluidity according to

176
$$\begin{bmatrix} \dot{\varepsilon}_1 \\ \dot{\varepsilon}_2 \\ \dot{\varepsilon}_3 \\ \dot{\varepsilon}_4 \\ \dot{\varepsilon}_5 \\ \dot{\varepsilon}_6 \end{bmatrix} = \begin{bmatrix} A_{11} & A_{12} & A_{13} & A_{14} & A_{15} & A_{16} \\ A_{21} & A_{22} & A_{23} & A_{24} & A_{25} & A_{26} \\ A_{31} & A_{32} & A_{33} & A_{34} & A_{35} & A_{36} \\ A_{41} & A_{42} & A_{43} & A_{44} & A_{45} & A_{46} \\ A_{51} & A_{52} & A_{53} & A_{54} & A_{55} & A_{56} \\ A_{61} & A_{62} & A_{63} & A_{64} & A_{65} & A_{66} \end{bmatrix} \cdot \begin{bmatrix} \sigma_1 \\ \sigma_2 \\ \sigma_3 \\ \sigma_4 \\ \sigma_5 \\ \sigma_6 \end{bmatrix} \cdot II_\sigma^{(n-1)/2}. \tag{5}$$

177 To solve eq. (5) for the strain rate, the material constant $\underline{A}$, which we will refer to as the

178 fluidity parameter tensor, must be known. $\underline{A}$ is a function of temperature and grain size, but

179 also depends on the crystal orientations of the aggregate. The micromechanical model of

180 Hansen et al. (2016a) allows us to find the stress needed to produce any strain rate for a given

181 olivine texture. Therefore, to find the components of $\underline{A}$ with the pseudo-Taylor mechanical

182 model, we need to apply 6 different strain rates to the aggregate and calculate the 6 stress

183 vectors that are required to produce these strain rates. The six strain rates define the columns

184 of the tensor $\underline{E}$,

185
$$E = \begin{bmatrix} \dot{\varepsilon}_0 & -\dot{\varepsilon}_0/2 & -\dot{\varepsilon}_0/2 & 0 & 0 & 0 \\ -\dot{\varepsilon}_0/2 & \dot{\varepsilon}_0 & -\dot{\varepsilon}_0/2 & 0 & 0 & 0 \\ -\dot{\varepsilon}_0/2 & -\dot{\varepsilon}_0/2 & \dot{\varepsilon}_0 & 0 & 0 & 0 \\ 0 & 0 & 0 & \dot{\varepsilon}_0/\sqrt{2} & 0 & 0 \\ 0 & 0 & 0 & 0 & \dot{\varepsilon}_0/\sqrt{2} & 0 \\ 0 & 0 & 0 & 0 & 0 & \dot{\varepsilon}_0/\sqrt{2} \end{bmatrix}, \tag{6}$$

186 where $\dot{\varepsilon}_0$ is the applied strain rate amplitude. By applying the micromechanical model of

187 Hansen et al. (2016a) separately to each column of $\underline{E}$, we can compute the set of stress tensors

188 associated with each of these six strain rates. We use these stress tensors to construct the

189 tensor $\underline{S}$, for which each row represents the stress vector associated with the strain-rate vector

190 in each column of $\underline{E}$, multiplied by $II_\sigma^{(n-1)/2}$. These two tensors are related according to the

191 equation

192 $\underline{E} = \underline{A} \cdot \underline{S}$, $\tag{7}$

193 where $\underline{S} =$

$$\begin{bmatrix} II_{\sigma_1}^{(n-1)/2}\sigma_{1_1} & II_{\sigma_1}^{(n-1)/2}\sigma_{2_1} & II_{\sigma_1}^{(n-1)/2}\sigma_{3_1} & II_{\sigma_1}^{(n-1)/2}\sigma_{4_1} & II_{\sigma_1}^{(n-1)/2}\sigma_{5_1} & II_{\sigma_1}^{(n-1)/2}\sigma_{6_1} \\ II_{\sigma_2}^{(n-1)/2}\sigma_{1_2} & II_{\sigma_2}^{(n-1)/2}\sigma_{2_2} & II_{\sigma_2}^{(n-1)/2}\sigma_{3_2} & II_{\sigma_2}^{(n-1)/2}\sigma_{4_3} & II_{\sigma_2}^{(n-1)/2}\sigma_{5_2} & II_{\sigma_2}^{(n-1)/2}\sigma_{2_2} \\ II_{\sigma_3}^{(n-1)/2}\sigma_{1_3} & II_{\sigma_3}^{(n-1)/2}\sigma_{2_3} & II_{\sigma_3}^{(n-1)/2}\sigma_{3_3} & II_{\sigma_3}^{(n-1)/2}\sigma_{4_3} & II_{\sigma_3}^{(n-1)/2}\sigma_{5_3} & II_{\sigma_3}^{(n-1)/2}\sigma_{6_3} \\ II_{\sigma_4}^{(n-1)/2}\sigma_{1_4} & II_{\sigma_4}^{(n-1)/2}\sigma_{2_4} & II_{\sigma_4}^{(n-1)/2}\sigma_{3_4} & II_{\sigma_4}^{(n-1)/2}\sigma_{4_4} & II_{\sigma_4}^{(n-1)/2}\sigma_{5_4} & II_{\sigma_4}^{(n-1)/2}\sigma_{6_4} \\ II_{\sigma_5}^{(n-1)/2}\sigma_{1_5} & II_{\sigma_5}^{(n-1)/2}\sigma_{2_5} & II_{\sigma_5}^{(n-1)/2}\sigma_{3_5} & II_{\sigma_5}^{(n-1)/2}\sigma_{4_5} & II_{\sigma_5}^{(n-1)/2}\sigma_{5_5} & II_{\sigma_5}^{(n-1)/2}\sigma_{6_5} \\ II_{\sigma_6}^{(n-1)/2}\sigma_{1_6} & II_{\sigma_6}^{(n-1)/2}\sigma_{2_6} & II_{\sigma_6}^{(n-1)/2}\sigma_{3_6} & II_{\sigma_6}^{(n-1)/2}\sigma_{4_6} & II_{\sigma_6}^{(n-1)/2}\sigma_{5_6} & II_{\sigma_6}^{(n-1)/2}\sigma_{6_6} \end{bmatrix}$$

194  In $\underline{S}$, $\sigma_{i_j}$ denotes the ith component of the deviatoric stress in Kelvin notation corresponding to

195  the jth column of $\underline{\underline{E}}$, calculated with the pseudo-Taylor method described by (Hansen et al.,

196  2016a), and $II_{\sigma_j}$ is the second invariant of each stress tensor (corresponding to the jth column

197  of $\underline{\underline{E}}$). Equation (7) needs to be inverted to determine $\underline{A}$. However, due to the

198  incompressibility criteria and because $\underline{\underline{S}}$ builds up by deviatoric stresses, $\sum_{i=1}^{3} E_{ij} = 0 \wedge$

199  $\sum_{i=1}^{3} S_{ij} = 0$ for each j. This means that $\underline{\underline{S}}$ is not invertible in its full form. However, we do

200  not lose information by reducing both $\underline{\underline{E}}$ and $\underline{\underline{S}}$ by one column and one row (the first column

201  and row) because the first component of both the strain rate and the deviatoric stress can be

202  reconstructed from their second and third components. This reduction yields $\underline{\underline{E}}'=\underline{\underline{A}}'\cdot\underline{\underline{S}}'$, where

203  each matrix has 5 rows and columns and a rank of 5. Hence, $\underline{\underline{S}}'$ is invertible, so

204  $\underline{\underline{A}}'=\underline{\underline{E}}'\cdot\underline{\underline{S}}'^{-1}$ $\hspace{6cm}$ (8)

205  can be solved.

206  Knowing the fluidity parameter tensor, $\underline{\underline{A}}'$, for a given olivine texture allows us to compute

207  the full strain-rate tensor for any given applied stress tensor. The actual deformation that is

208  produced depends on model assumptions about how this deformation is geodynamically

209  expressed in the rock. In this study, we examine geodynamic processes associated with simple

210  shear of the asthenosphere, e.g., as produced by the motion of a surface plate over an

211  asthenospheric layer (Figure 1). To implement this deformation, we impose a deformation

212  gradient consistent with simple shear, for which the deformation tensor ($D_{ij} = \partial u_i / \partial x_j$) is

213  $D_{F_1} = \begin{bmatrix} 0 & 2\dot{\varepsilon}_{12} & 2\dot{\varepsilon}_{13} \\ 0 & 0 & 2\dot{\varepsilon}_{23} \\ 0 & 0 & 0 \end{bmatrix}$ $\hspace{5cm}$ (9)

214  for the case in which the asthenosphere is sheared with force $F_1$ (*Fig. 1*) and thus driven by a

215  stress $\sigma_{13}$. The deformation that results is described in (9) by $D_{12}$, $D_{23}$, and $D_{13}$, where $D_{12}$ and

216  $D_{23}$ are only excited because of the anisotropic nature of the rheology. Note that we neglect

217  the normal strain rate components ($D_{11}=D_{22}=D_{33}=0$) assuming that the geometric constraints

218  on the system do not permit net elongation or contraction in any direction. From the imposed

219  deformation, we can calculate the associated texture evolution as a function of time for a

220  given applied stress history. The time-step in the calculation is set based on the strain rate to

221  have 0.1 strain increment for each time-step, which we have found to produce stable results.

**2.2 Geodynamic model**

223    To investigate the influence of anisotropic viscous behavior in geodynamic scenarios with

224    changing orientations of stress, we model the deformation of a set of olivine grains

225    representing the behavior of the asthenosphere. We apply a shear stress (=force/area) of 0.68

226    MPa, which roughly corresponds to the shear stress acting on a plate of area 6000 km by 6000

227    km that is necessary to balance an edge force of $4.1 \cdot 10^{12}$ N/m (a lower bound estimate for

228    the value of slab pull force transferred to the plate from the negative buoyancy of a

229    subducting oceanic lithosphere; Schellart, 2004) above a 200-km-thick asthenosphere (*Fig.*

230    *1A*). We track the deformation of the asthenosphere using the micromechanical model of

231    texture-development and viscous anisotropy described above. Based on the anisotropic

232    properties of a representative olivine aggregate, we compute the strain rate within the

233    asthenosphere, and associated parameters such as plate speed and movement direction, all as a

234    function of time, accumulated strain, and olivine texture development. To calculate the plate

235    velocity, we assume that the velocity is 0 at the base of the $H_a = 200$ km thick asthenosphere

236    and that the horizontal velocity at the top of the asthenosphere is the plate velocity, hence

237    $$V_{plate} = 2 \cdot \sqrt{\dot{\varepsilon}_{13}^{2} + \dot{\varepsilon}_{23}^{2}} \cdot H_a \qquad (10)$$

238    To investigate different deformation paths that are analogs for a variety of upper mantle

239    processes, we change the orientation of the applied shear stress, and consequently the

240    deformation applied to the asthenosphere, at a chosen instant after an olivine texture has

241    formed (*Fig. 1B*). Such a change could be induced by a change in the external driving forces

242    applied to the asthenosphere. An intuitively simple approach would be to rotate the imposed

243    driving stress relative to the texture that initially formed. However, for numerical and

244    analytical simplicity, we instead rotate the olivine texture with respect to the imposed stress

245    (as shown in *Fig. 1C*), which is held steady. This approach produces an equivalent result and

246    allows us to keep the definition of both the shear stress and the deformation tensors (equation

247    9) unchanged. Later, we will discuss the geodynamic scenarios represented by the various

248    rotations of the olive texture with respect to the applied shear stress.

249    We define the angles $\alpha$ and $\beta$ as the orientations of the imposed shear stress and the resulting

250    plate motion with respect to a coordinate system fixed in the asthenosphere (x-axis, *Fig. 1C*).

251    Thus, $\alpha$ is the angle between the (1)-axis (which is the same as the direction of the shear

252    stress) and the x-axis (which is the angle of rotation of the texture) in *Fig. 1*, and $\beta$ is the angle

253  between the plate motion direction and the (x)-axis. The horizontal shear components of the

254  strain rate ($\dot{\varepsilon}_{23} \wedge \dot{\varepsilon}_{13}$) are used to calculate the direction of the plate movement (*β*), as follows:

255  $$\beta = atan\left(\frac{\dot{\varepsilon}_{23}}{\dot{\varepsilon}_{13}}\right) + \alpha \qquad\qquad\qquad (9)$$

## 3. Results

257  We present the results of 27 models with different deformation paths. Each model result is an

258  average of 5 individual runs, each initiated with 1000 olivine grains with initial orientations

259  randomly drawn from a uniform distribution. Therefore, we effectively represent the

260  asthenosphere under a large (6000x6000 km$^2$) plate using the average of 5 model runs of 1000

261  grains each.

### 3.1. Monotonic simple shear

263  First, we present the evolution of asthenospheric strain rates and olivine texture development

264  from a uniformly distributed texture (i.e., an isotropic mantle) to a well-developed texture

265  (anisotropic, weak mantle). As the mantle accumulates strain, the a-axes of olivine rotate

266  towards the shear direction *(Fig. 1B)*, developing a texture that decreases the effective

267  viscosity of the asthenosphere and, therefore, increases the velocity of the plate. We examined

268  two sets of models differing only in the randomly created uniformly distributed orientations at

269  the start of the models (*Fig. 2*, black and grey curves). The similarity of these two model

270  averages implies that the average of model runs with 5x1000 grains gives a reasonably stable

271  result. However, subtle differences in the initial textures of the two models can still cause

272  minor differences in the amplitudes of the fluidity parameters (*Fig. 2B*).

273  The amplitude of the shear strain rate ($|\dot{\varepsilon}| = 2 \cdot \sqrt{\dot{\varepsilon}_{12}^2 + \dot{\varepsilon}_{13}^2 + \dot{\varepsilon}_{23}^2}$, simply referred to as

274  strain rate hereafter) exhibits characteristic variations throughout this deformation (*Fig. 2*),

275  which result from the texture evolution of the olivine aggregates and the associated changes in

276  the fluidity parameter tensor (*Fig. 2B and 2C*). With an initially uniform olivine distribution,

277  the strain rate in the asthenosphere is 1.5-1.7·10$^{-14}$ s$^{-1}$, which corresponds to a plate velocity of

278  ~9.5-10.5 cm/yr velocity. As accumulated strain increases, the olivine texture develops, the

279  effective viscosity of the asthenosphere decreases, and the plate velocity increases, reaching a

280  maximum of 14.8 cm/yr (2.4·10$^{-14}$ s$^{-1}$) around a strain of 8, i.e. after ~14 Myr of shearing.

281  With further shearing, the plate velocity decreases and subsequently stabilizes at 12.3 cm/yr

282  (1.9·10$^{-14}$ 1/s). The effective viscosity is inversely proportional to the strain rate, reaching a

283  minimum at ~14.5 Myr (strain of 8) and slightly increasing during the later history. The

284    magnitude of the viscosity varies from 2.9-4.5 x10$^{19}$ Pa·s. Hence, with continuous shearing,

285    any further evolution of the olivine texture decreases the asthenosphere's effective viscosity

286    by less than a factor of 2.

287    Both the shear components of the fluidity tensor ($A_{44}$, $A_{55}$, $A_{66}$ in *Fig. 2B*) and the off-diagonal

288    components ($A_{45}$ and $A_{65}$ in *Fig. 2C*) exhibit variations with time as the olivine texture

289    develops. The non-zero component of the stress tensor is $\sigma_{13}$, ($\sigma_5$ in Kelvin notation), which

290    means that $A_{55}$ represents the fluidity in the shear direction (shearing on the (3) plane in the

291    (1) direction, creating $\partial v_1/\partial x_3$). Note that since $\sigma_{31} = \sigma_{13}$ (symmetry of the stress tensor),

292    then $A_{55}$ also represents the fluidity for the reciprocal deformation (i.e., shearing on the (1)

293    plane in the (3) direction, creating $\partial v_3/\partial x_1$). $A_{44}$ and $A_{66}$ represent the values of the fluidity

294    that would control the deformation (shearing given by $\partial v_3/\partial x_2$ or $\partial v_2/\partial x_3$ for $A_{44}$ and by

295    $\partial v_1/\partial x_2$ or $\partial v_2/\partial x_1$ for $A_{66}$) if we were to change the shear stress to $\sigma_{23}$ ($=\sigma_{32}$) or $\sigma_{12}$

296    ($=\sigma_{21}$), respectively.

297    Initially, there is no preferred orientation of the olivine grains, and the three shear fluidity

298    components are the same. As the asthenosphere deforms and the texture develops in

299    association with shearing on the (3) plane in the (1) direction, $A_{55}$ increases, which is

300    associated with a decrease in viscosity and an increase in the plate velocity. In contrast, the

301    fluidity component $A_{44}$ ($A_{2323}$) decreases, which indicates that it would become harder and

302    harder to shear the asthenosphere with a stress $\sigma_{23}$, which would induce shearing on the (3)

303    plane in the (2) direction (i.e., plate motion in a perpendicular direction), or reciprocally on

304    the (2) plane in the (3) direction. Surprisingly, $A_{66}$ increases with progressive deformation,

305    and most of the time is even larger than $A_{55}$. Thus, as the texture develops, it also becomes

306    easier to shear the asthenosphere along the vertical (*2*) plane in the (3) direction (or,

307    reciprocally, along the (3) plane in the (2) direction). The $A_{45}$ and $A_{65}$ off-diagonal

308    components (*Fig. 2C*) are noteworthy because these components couple $\sigma_{13}$ to $\dot{\varepsilon}_{23}$ and $\dot{\varepsilon}_{12}$,

309    respectively (eq. 5). These components are initially zero, but do take on finite values with

310    progressive deformation. In other words, as the anisotropy of the system develops, the applied

311    shear stress begins to induce shear strains on planes other than the primary shear plane, and in

312    directions other than the primary shear direction. However, because these components are two

313    orders of magnitude lower than $A_{55}$, the strain rate in this simple case is dominated by the

314    effects of $A_{55}$. Consequently, values of $A_{55}$ (*Fig 2B*), strain rate (*Fig. 2D&E*), and plate

315    velocity (*Fig. 2D*) all exhibit the same trend as a function of time and strain.

316

### 3.1.1. Rheology and texture parameters

As demonstrated above, the plate velocity (calculated from the horizontal strain rate) and the shear-parallel ($A_{55}$) component of the fluidity tensor are linearly dependent, and those terms are inversely proportional to the effective viscosity. To further understand the initially increasing and subsequently decreasing evolution of the strain rate, the relationship between the texture and the rheological behavior of the asthenosphere (olivine aggregate) needs to be examined. In the literature, a number of texture parameters have been proposed to quantify the orientation distribution of a group of crystals. For example, the J-index (also referred to as the texture strength) provides a metric for the degree of alignment of crystal orientations (Bunge, 1982), varying between 1 (uniform distribution) and infinity (single-crystal texture). The M-index (Skemer et al., 2005) also assesses the degree of alignment and results from the difference between the uncorrelated and the uniform misorientation-angle distributions, with a value between 0 (uniform distribution) and 1 (single-crystal texture). We calculated both the J- and the M- indices with MTEX (Mainprice et al., 2015) and plotted the latter along with the plate velocity against the accumulated strain (*Fig. 3A*). Comparing the two curves (blue and yellow, for the plate velocity and the M-index, respectively), no direct relationship is observable.

We examine the subtleties of the textural development with pole-figures that indicate the orientation distributions of the three main axes of the olivine grains (*Fig.3*). These plots illustrate that better correlation may be found between the plate velocity and the distributions of individual axes instead of the M-index, which describes the orientation distribution of all three axes. For example, as the plate velocity decreases between the strains of 8 and 16, the distributions of the a- and c-axes become more girdled, while the distribution of the b-axes becomes more clustered, resulting in an increasing M-index. Thus, the qualitative comparison of the pole figures with the plate velocity suggests that the distribution of a-axes, which represents the easiest slip direction, exerts a primary influence on the rheological behavior of the aggregate.

Therefore, we calculate three additional parameters that describe the degree to which the orientation distribution is random (*R*), girdle-like (*G*) or point-like (*P*), for each crystallographic axis (a-axes: *P-a, G-a, R-a*; b-axes: *P-b, G-b, R-b*; c-axes *P-c, G-c, R-c*) (Vollmer, 1990). All three parameters vary between 0 and 1, and the sum of all three parameters is 1 for each axis distribution. We plot these texture parameters against the accumulated strain and the plate velocity (*Fig. 3A*), revealing some correlation between the *P-*

350  *a* values and the plate velocity and some anticorrelation between the *G-a* values and the plate

351  velocity.

352

### 3.2.    Change in the direction of the shear force

354  The aim of this section is to test several deformation paths that, to first order, represent those

355  expected for different geodynamic processes. For example, changing the force acting on the

356  plate from the (1) direction to the (2) direction (i.e., from force $F_1$ to force $F_2$ in *Fig. 4*)

357  represents a change in the direction of the pull force acting on a tectonic plate, and should

358  change the direction of plate movement (*Fig. 4*). Other changes to the force that we explore

359  are illustrated in Fig. 4. These force directions can mimic shearing induced by subduction

360  initiation and/or dripping ($F_3$ and $F_5$) or the start of transform faulting ($F_4$ and $F_6$).

361  First, we describe the results of an instantaneous change in the direction of the asthenospheric

362  shear force (from $F_1$ to $F_2$, $F_3$, $F_4$, $F_5$, or $F_6$ in *Fig. 4*). We then examine the influence on the

363  deformation behavior of (1) the rate of rotation of the shear force direction (from 1 Myr/90° to

364  12 Myr/90°), (2) the amount of texture development prior to the change, and (3) the total

365  rotation angle of the driving stress when switching from $F_1$ to $F_2$. As noted above, we

366  implement a change in the driving force (or shear stress) by rotating the textured olivine

367  aggregate (formed by applying the shear of model 1 for a chosen amount of accumulated

368  strain) while keeping the shear stress constant (*Fig. 1C*).

369      3.2.1 Instantaneous change in shear direction

370  At a strain of 8 (i.e., after shearing the olivine aggregate for 14.5 Myr), the a-axes distribution

371  reaches the maximum value of *P* (*Fig. 3*). Hence, to maximize the effect of anisotropy in our

372  tests, we first reach a shear strain of 8 by applying $\sigma_{13}$ with deformation consistent with

373  applying the force $F_1$ (using the same initial texture as in model 1), then switching to a new

374  force direction (defined in *Fig. 4*). Due to the symmetric nature of the stress tensor, $F_3$ is

375  achieved using the same applied stress as $F_1$, but by employing different applied boundary

376  conditions that enforce deformation consistent with vertical shearing, i.e.: $D_{F_3} =$

377  $\begin{bmatrix} 0 & 0 & 0 \\ 2\dot\varepsilon_{12} & 0 & 0 \\ 2\dot\varepsilon_{13} & 2\dot\varepsilon_{23} & 0 \end{bmatrix} = D_{F_1}{}^T$. $F_2$ and $F_5$ are consistent with a stress tensor in which only $\sigma_{23}$ and

378  $\sigma_{32}$ are non-zero and deformation is given by $D_{F_2} = \begin{bmatrix} 0 & 0 & 2\dot\varepsilon_{13} \\ 2\dot\varepsilon_{12} & 0 & 2\dot\varepsilon_{23} \\ 0 & 0 & 0 \end{bmatrix} \wedge D_{F_5} = D_{F_2}{}^T$. $F_4$ and

379    $F_6$ are both consistent with a stress tensor where only $\sigma_{12}$ and $\sigma_{21}$ are non-zero and induce

380    deformation given by $D_{F_4} = \begin{bmatrix} 0 & 2\dot{\varepsilon}_{12} & 2\dot{\varepsilon}_{13} \\ 0 & 0 & 0 \\ 0 & 2\dot{\varepsilon}_{23} & 0 \end{bmatrix} \wedge D_{F_6} = D_{F_4}{}^T$. As mentioned before, these

381    deformations are equivalent to those achieved by rotating the mantle (i.e. the olivine

382    aggregate) with respect to the force $F_1$ and keeping the imposed boundary conditions

383    expressed by the deformation tensor $D_{F_1}$ (equation 9). A 90° rotation of the aggregate around

384    the x-axis represents a change from $F_1$ to $F_4$, around the y-axis reproduces $F_3$, and around the

385    z-axis reproduces $F_2$. $F_5$ is modeled by rotating the aggregate around the x- and then z-axes,

386    and $F_6$ is modeled by rotation around the x- then y-axes. Referring to *Fig. 4*, rotating the

387    aggregate around its x or its x then y axes represents shearing produced by a transform fault

388    ($F_4$ or $F_6$), rotation around the y or the x then z axes represents shearing associated with

389    dripping or subduction ($F_3$ or $F_5$), while rotation around the z axis represents a change in the

390    direction of the horizontal shear ($F_2$) (e.g., due to a change in the direction of slab pull force).

391    The effect of changing the shear direction largely depends on the direction of the new shear

392    stress with respect to the textured mantle (*Fig. 5*). For example, when the rotation results in a

393    new shear stress that primarily induces deformation on the hardest (010)[001] slip system ($F_2$

394    or $F_5$), the strain rate decreases dramatically, from $2.3 \cdot 10^{-14}$ to $4.9 \cdot 10^{-15}$ s$^{-1}$ (*Fig. 5B*, orange

395    and green curves). Translating to plate velocity, this change implies a decrease from 14.8

396    cm/yr to 3 cm/yr.

397    Note that reciprocal pairs of shear deformations (that is, $F_1$-$F_3$, $F_2$-$F_5$, and $F_4$-$F_6$) are

398    associated with the same stress state (shear stress given by $\sigma_{13}$, $\sigma_{23}$, $\sigma_{12}$, respectively) and

399    initially activate the same slip systems because they are deforming the same initial texture.

400    Thus, the effective viscosity, and the associated deformation rates, for each of these pairs is

401    initially the same (as shown at a strain of 8 in *Figs. 5A, 5B, and 5C*, respectively). However,

402    because the rotation associated with these deformation pairs is different (because we employ

403    different boundary conditions D), the textures for these pairs evolve differently (*Fig. 5*, right

404    column), and their strain-rates diverge (*Fig. 5*, left column).

405                    *3.2.1.1 Representing change in plate motion direction*

406    Rotating the olivine aggregate around its z-axis represents a relative change in the direction of

407    the plate driving force. The result of a model with 90° instantaneous rotation (green curve in

408    *Fig. 5B*) exhibits a dramatic reduction in strain rate and a slow recovery of the olivine texture

409    after the rotation. By the end of the model run (total shear strain of 21) the strain rate has

410 increased to $1.3 \cdot 10^{-14}$ s$^{-1}$, which is still less than the strain rate for the initially isotropic

411 aggregate. Because of the slow deformation associated with the diminished strain rate, this

412 partial recovery took almost 50 Myr. Examination of the change in olivine texture directly

413 after the rotation (at strain of 8.5, *Fig. 5*) illustrates that the orientations are well organized but

414 that the preferred orientation is perpendicular to the direction of shearing (*Fig. 5*). When the

415 strain rate finally starts to increase, the a-axis distribution is more random or girdle-like rather

416 than point-like, even at a total strain of 21. Regarding the fluidity tensor, when the texture is

417 rotated, the $A_{55}$ component (which relates $\sigma_{13}$ to $\dot{\varepsilon}_{13}$) decreases while both $A_{45}$ and $A_{65}$ exhibit

418 a minor increase, leading to similar values for all three components.

### *3.2.1.2 Shear forces associated with transform faults*

420 There are two possibilities for creating shear stress in a horizontal direction along a vertical

421 plane, which roughly approximates the stress state associated with a transform fault. The

422 possible shear forces are $F_4$ or $F_6$ (*Fig. 4*), which produce very different paths in the strain-rate

423 evolution (*Fig. 5C*) if there is already a well-developed texture associated with deformation

424 due to $F_1$. At the time of rotation (at a strain of 8), both models exhibit an elevated strain rate

425 (to $3.3 \cdot 10^{-14}$ s$^{-1}$) compared to the earlier deformation (driven by $F_1$). The pink curve,

426 representing the switch from $F_1$ to $F_4$, after the initial peak strain rate, slowly decreases to

427 ~$1.5 \cdot 10^{-14}$ s$^{-1}$. Switching from $F_1$ to $F_6$ is relatively easy, as the model exhibits increasing

428 strain rate (up to ~$6.7 \cdot 10^{-14}$ s$^{-1}$) associated with the texture evolution after the rotation for an

429 additional shear strain of ~4 (*Fig. 5C*, dark blue curve). This peak is followed by a quickly

430 decreasing strain rate that stabilizes around ~$2 \cdot 10^{-14}$ s$^{-1}$, which is comparable to the strain rate

431 for larger strains in reference model 1 (black curve). The high strain rate produced by the

432 model representing $F_6$ is associated with a quick texture evolution and a point-like

433 distribution in the new shear direction that is more strongly aligned than the distribution prior

434 to the change in shear direction. In contrast, changing from $F_1$ to $F_4$ (rotation around the *x*-

435 axes) keeps the a-axis distribution basically aligned with the shear direction, but with

436 subsequent strain, the a-axis distribution forms a girdle, decreasing the initial point-like

437 distribution and leading to slower strain rates than prior to the change in shear direction.

### *3.2.1.3 Shear forces associated with dripping/subduction*

439 There are two possibilities for creating shear stress in a vertical direction as a rough

440 approximation of the stress state associated with subduction or dripping instabilities.

441 Changing from $F_1$ to $F_3$ (texture rotation around the *y*-axis; *Fig. 4*), results in initial

442 deformation occurring at the same rate as for $F_1$ (because $F_1$ and $F_3$ are reciprocal

443 deformations, as described above) followed by a decrease in strain rate (i.e. small increase in

444 the effective viscosity) as the texture evolves (*Fig. 5A*, cyan curve). Subsequent texture

445 evolution produces a period with increasing strain rate, between strains of 8.5 (0.5 after the

446 switch) to 13, peaking at $4.4 \cdot 10^{-14}$ s$^{-1}$. The model results exhibit a decreasing trend in strain

447 rate immediately after this peak, reaching a final strain rate of $2 \cdot 10^{-14}$ s$^{-1}$ (after a total strain of

448 21). In contrast, changing from $F_1$ to $F_5$ (orange curve in *Fig. 5B*) induces a dramatically

449 diminished strain rate ($5 \cdot 10^{-15}$ s$^{-1}$, equivalent to that produced by $F_2$ as described above) that

450 slowly recovers over the next 20-25 Myr (by a total strain of 14) and stabilizes around 2.2-

451 $2.3 \cdot 10^{-14}$ s$^{-1}$, which is slightly higher than the strain rate at high stresses in model 1. Similar to

452 the "transform fault" models, the strain-rate curves for "subduction/dripping" can be linked to

453 the texture development. The higher strain rate at the end of the model that applies $F_5$ (*x*- then

454 *y*- rotation) compared to the model end after applying $F_3$ results from a more point-like

455 distribution of the olivine a-axes (*Fig. 5A&B*).

456         3.2.2. Rate of rotation of the stress orientation

457 In the preceding section, the change in texture orientation relative to the applied forces was

458 instantaneous. In the following sections, the rate, timing, and amount of rotation of the olivine

459 aggregate are examined. Here we focus on the simplest case, a change in the plate-motion

460 direction ($F_1$ changing to $F_2$). Here, we impose a 90° rotation over a time interval ranging

461 from 1 to 13 Myr, after ~14 Myr of initial shearing (an accumulated strain of 8).

462 As described above, we use $\alpha$ and $\beta$ (eq. 9) to indicate the angle between the x-axis (in the

463 aggregate reference frame) and the shear force and plate motion directions, respectively.

464 During rotation of the aggregate, $\alpha$ linearly changes with time from 0° to -90°. In contrast, the

465 angle $\beta$ does not change linearly with time and can differ from $\alpha$ significantly because the

466 olivine texture excites plate motion differently in varied directions. During the rotation period,

467 and independently of its duration, the plate movement differs from the shear direction by up

468 to 20° (*Fig. 6A*). Minor differences can be observed depending on the rotation rate. Once 90°

469 rotation is achieved, the plate movement is either parallel to the shear direction (1 and 10 Myr

470 rotation period), overturned (3 and 5 Myr rotation period) or rotated less than the shear

471 direction (13 Myr rotation period). After rotation, all models evolve in a similar manner,

472 resulting in velocity vectors 15-20° away from the shear direction. The plate speed drastically

473 decreases, reaching 3 cm/yr by the end of the rotation period (*Fig. 6B*). As in the

474 instantaneous rotation model, the plate movement cannot recover its original rate after the

475    rotation (*Fig. 6B*). The models with shorter rotation time (1-5 Myr) reach a maximum of 7

476    cm/yr while the models with longer texture rotation time (10-13 Myr) reach a maximum of 5

477    cm/yr by the end of the model (at strain ~ 20-21). Interestingly, during the first ~4° of

478    rotation, the plate velocity increases, except for the model with 1 Myr rotation time, where the

479    rotation step is 9°/timestep (as the timestep is fixed to 100 kyr during the rotation). This

480    increase can be explained by the mean orientation of the olivine texture (see pole figures for a

481    strain of 8 on *Fig. 3*) and the plate movement (*Fig. 6A*) before the onset of rotation, which are

482    both a few degrees (~ 4° and -1.2°, resp.) offset from the shear direction. Hence, at the onset

483    of rotation, the texture initially becomes more aligned with the shearing, resulting in up to 2

484    cm/yr increase in the plate velocity (see texture evolution animations, which are available in

485    the supplementary materials for each model).

486           3.2.3. Role of texture evolution prior to the rotation

487    In an additional series of calculations, we varied the amount of accumulated strain between 2

488    and 14 prior to a 90° rotation, which was implemented using two different rotation rates (90°

489    and 9°/Myr).

490    The magnitude of the velocity decrease associated with rotation appears to be proportional to

491    the textural maturity of the aggregate before rotation (*Fig. 7B*). However, the rate of rotation

492    has only a small effect, as described previously (*Fig. 6*). Note that for the models in which the

493    rotation is imposed after a strain of 11 or 14, faster rotation results in a slightly lower

494    minimum plate velocity (*Fig. 7D*). Only the model with fast and early rotation (rotation at a

495    strain of 2) exhibits velocities that return to the original plate velocity magnitude, while the

496    other models reach strain of 21 with only 5.4-8.4 cm/yr plate velocity (*Fig. 7B*).

497    A large range of variation in the plate motion direction can be observed depending on the

498    amount of initial strain, rotation rate, and time/total accumulated strain (*Fig. 7A & C*). In most

499    of the models, the difference $\alpha$-$\beta$ grows from ~-1° to ~15-20° during rotation (see the two

500    outlined circles in each line on *Fig.7C*), which is also the maximum difference between $\alpha$ and

501    $\beta$. There are three slight outlier models, in which extreme magnitudes of $\alpha$-$\beta$ occur during the

502    model evolution. With an initial strain of 5 and a slow-rotation rate, the plate motion direction

503    can differ from the shear direction by up to 29°, while in the models in which an initial strain

504    of 14 is imposed, the plate-motion direction rotates more than the shear direction, reaching

505    extremes of -6 ° and -21° (with 1 and 10 Myr rotation time, respectively).

506    3.2.4. Role of the amount of rotation

507 In more realistic geodynamic scenarios, the driving forces on plates are unlikely to rotate as

508 much as 90°, so we additionally tested a range of rotations from 22° to 90° degrees with slow

509 (9°/Myr) and fast (90°/Myr) rotation rates. In all of these models, the aggregate was sheared

510 with force $F_1$ until a strain of 8 prior to the rotation. We found (*Fig. 8*) that the larger the

511 rotation, the lower the average strain rate, and therefore the lower the average plate velocity

512 (*Fig. 8B&D*). Furthermore, the models with faster rotation rates exhibit a greater variability of

513 plate motion directions and velocities than the models with slower rotation rates (*Fig. 8*).

514 With only 22° rotation, $\beta$ differs from $\alpha$ by only 15° during the rotation in both models, and

515 this difference linearly decreases as the model progresses until, at the end of the model, the

516 plate motion becomes parallel to the shear direction. The plate velocity decreases to 7.5-7.8

517 cm/yr, which then climbs back to the isotropic rate (~10 cm/yr) by the end of the models. If

518 the total change in shear direction is 45° or more, all models result in ~20° difference between

519 $\alpha$ and $\beta$ during the rotation, independent of the rate of rotation. Later, the models with slower

520 rotation rate result in even larger differences between $\alpha$ and $\beta$. The plate motion direction can

521 change more quickly if the plate velocity is high, such as in the model with 45° rotation at

522 90°/Myr during the period between 25 and 35 Myr (*Fig. 8B*). On the other hand, in the model

523 with 67° rotation at 9°/Myr, the plate velocity remains between 3.5-5 cm/yr, and $\alpha$-$\beta$ remains

524 ~20° (15-25°).


525 **4.** *Discussion*

526 The results described above suggest that the effective viscosity and strain rate of the

527 asthenosphere, and the associated plate velocity at the surface, are extremely sensitive to the

528 olivine texture. The asthenosphere weakens as the olivine texture develops with the a-axes

529 parallel to the shear direction ('anisotropic weak' on *Fig. 1B*), allowing for a 40% increase in

530 plate velocity (or equally, decrease in effective viscosity). The asthenosphere acts 'strong'

531 (*Fig. 1C*) if the mean a-axes direction is perpendicular to, and the mean c-axes direction is

532 parallel to, the shear direction. In this case, the effective viscosity is up to ~5 times higher

533 than if the a-axes are parallel to the shear force, resulting in a slower plate velocity that is only

534 a third of the velocity over the isotropic asthenosphere and a fifth of that in the 'anisotropic

535 weak' case (Fig. 10). This difference in viscosity is in accordance with the differences in the

536 strengths of the slip systems (Table 1 in Hansen et al., 2016a), favoring deformation parallel

537 to the a-axes (i.e. on the (010)[100] and (001)[100] slip systems, with strengths of 0.3 and

538   0.27, respectively) versus parallel to the c-axes (where the strength of the (010)[001] slip
539   system is 1.29). Thus, deformations that dominantly activate the (010)[100] slip system (e.g.,
540   $F_1$ and $F_3$ at a strain of 8, *Fig. 5A*) and the (001)[100] slip system (e.g., $F_4$ and $F_6$ at a strain of
541   8, *Fig. 5C*) exhibit much faster strain rates compared to those that dominantly activate the
542   (010)[001] slip system (e.g., $F_2$ and $F_5$ at a strain of 8, *Fig. 5B*).

543   The evolution of the plate velocity and plate-motion direction (or the entire matrix of $\dot{\varepsilon}$) is a
544   function of the olivine texture, which evolves due to the deformation. Hence the
545   asthenospheric rheology depends on the kinematics and vice-versa. Indeed, the models with
546   an instantaneous change in the force direction demonstrate that applying the same stress but
547   with different velocity boundary conditions (i.e. enforcing deformations consistent with
548   individual forces on the asthenosphere, as shown on *Fig. 4*) can produce very different strain
549   rate histories (e.g. *Fig. 5,* right column). For example, after creating a texture by force $F_1$,
550   switching to $F_2$ or $F_5$ both involve the same new stress state and both initially activate the
551   same (010)[001] slip system. Thus, both deformations initially produce the same (although
552   much reduced) strain rate (Fig. 5B). However, enforcing shear deformation in the vertical
553   direction (i.e. by $F_5$) allows for faster rotations of the olivine grains into the new shear
554   direction, allowing for higher strain rates as the texture develops.

555   Without changes in the shear force direction, the plate-velocity evolution follows a similar
556   trend to the values of *P-a* (point-like distribution value for the olivine a-axes) (*Fig. 3*).
557   However, if the direction of the shear force changes, this correlation is less clear. We
558   calculated the texture parameters described in section 3.1.1 for each model for a 0.5 strain
559   increment, for which an example is presented in *Figure 9*. If the texture is rotated 90° around
560   the z-axis with respect to the shear stress (in 1 Myr), then the changes in the values of *P*-a are
561   no longer correlated to the changes in the plate velocity, especially around the time of the
562   rotation (between a strain of 8 and 11), at which point the values of *P* for the a-, b-, and c-axes
563   (*P-a, P-b, P-c*) and the M-index are the largest (*Fig. 9*), while the plate velocity is the lowest.

564   To analyze the overall relationship between texture parameters and kinematic parameters (e.g.
565   plate velocity), we performed a Pearce correlation for all the models representing shearing by
566   plate pull. The correlation values between the plate velocity and texture parameters (*Fig. 9*)
567   demonstrate that the mean orientation of the olivine a-axes (*ori-a* on *Fig. 9*) as well as the
568   mean orientation of the c-axes (*ori-c*) are highly anticorrelated with the plate velocity. In
569   contrast, *P-a* has the highest correlation with the plate velocity of 0.64, which is similar to the
570   strength of the anticorrelation between the G-value (girdle-like distribution) of the a-axes (*G-*

571     *a*) and the plate velocity ($v_{plate}$). It is important to note that these parameters are not

572     independent from each other, as *G-a* and *P-a* are anticorrelated with a coefficient of -0.94

573     (similarly, -0.83 between *G-b* and *P-b*) and a 0.85 correlation between *ori-a* and *ori-c* (*Suppl.*

574     *Fig. S1*). Based on the correlation between the texture parameters and the plate velocity, as

575     well as between each pair of texture parameters, we find that the plate velocity can be linked

576     essentially to two parameters, the mean orientation and the value of *P* for the distribution of

577     the a-axes of the olivine grains, and therefore we see the strongest correlation between the

578     plate velocity and the product of those two parameters (*P-a ·cos(ori-a) in Figure 9*).

579     The need to consider both mean orientation and value of *P* for the a-axes provides important

580     context for comparison to previous investigations of texture evolution in olivine. Boneh et al.

581     (2015) used DRex, a different model of texture evolution (Kaminski and Ribe, 2002), to

582     investigate the influence of changing the deformation kinematics on texture. By examining

583     scenarios similar to our cases $F_2$ and $F_3$, Boneh et al. (2015) concluded that olivine texture

584     evolves to a new steady state by a shear strain of ~4. This conclusion was based on tracking

585     the dominant a-axis orientation, and is consistent with our observations (Fig. 5). However,

586     our investigation of the mechanical response of an olivine aggregate suggests that the

587     evolution of the viscosity can be considerably more protracted (especially for $F_2$), and our

588     correlation analysis demonstrates that additional features of the texture, most notably *P-a,* are

589     likely responsible for that difference.

590     The orientation of the olivine grains also exerts an important control on the direction of the

591     plate motion (or asthenospheric flow) with respect to the driving force. As noted above, in the

592     case of continuous shearing in one direction, the shear stress induces very little non-parallel

593     shear strain, but as soon as the shear direction is changed toward the mean orientation of the

594     olivine c-axes (i.e. the strongest slip system), we observe an increase in strain rates in

595     directions that are non-parallel to the shear stress. While the relationship between these

596     factors is not straightforward, it is clear that as *ori-a* starts to differ from the shear direction,

597     there is a corresponding change in the plate-motion direction (*Fig. 7 & 8*). The highest values

598     of *β* (plate-motion direction) occur at times in which *ori-a* differs 30-60° from the shear

599     direction. When this angle is higher, *β* decreases to ~0°, and the plate velocity slows

600     considerably. This behavior occurs because it is not possible to create strain perpendicular to

601     the forcing. Thus, when a grain is oriented such that the a-axis is perpendicular to the shear

602     direction, the easiest slip system cannot be activated (*Suppl. Fig. S2*).

## 5. *Relevance to natural phenomena*

Although our models are simplistic by nature, we can use them to gain some intuition about how viscous anisotropy may affect different geodynamic processes. However, before we proceed, it is important to note the limitations of our models. In particular, we have assumed that the asthenosphere under a large (6000x6000 km$^2$) plate deforms uniformly, and therefore the olivine texture, and its associated rheology, changes uniformly under the entire plate. Certainly, we may expect some textural heterogeneity for most realistic geodynamic scenarios, and this complexity may localize or otherwise change deformation patterns, affecting the results. Furthermore, our assumption that deformation occurs in a 200-km thick homogeneous layer of asthenosphere does not account for the possibility that deformation may be shifted to deeper layers if asthenospheric textures act to increase the asthenosphere's effective viscosity. Indeed, such a scenario is consistent with layered anisotropic textures under continents (e.g., Yuan and Romanowicz, 2010) and oceans (e.g., Beghein et al., 2014). Furthermore, other factors not included in our model, such as the presence of melt or strain localization, may affect deformation and/or textural development. As an example, our model also does not explicitly account for dynamic recrystallization, which Signorelli and Tommasi, (2015) showed can slightly increase the rate of fabric realignment relative to models with no recrystallization. However, our model parameters are calibrated based on laboratory experiments that inherently include such recrystallization (Hansen et al., 2016a, 2016b), and therefore, any application of this model assumes that rates of dynamic recrystallization are similar to those in laboratory experiments.

Despite these caveats, our simple experiments suggest that the textural anisotropy of the mantle should be associated with directional differences in effective viscosity that can be large (up to order of magnitude) and can change with time as textures develop. Anisotropic viscosity should thus influence a range of different geodynamic processes, and we can use our simple models to identify these influences (*Fig. 10*). In particular, depending on the orientation of the tectonic force with respect to the mean orientation of the olivine grains, and with respect to the three slip systems that can accommodate deformation, the anisotropic texture may either assist or resist continued deformation for a given process. This means that anisotropic viscosity may facilitate certain types of tectonic processes and impede others. We can thus use our simple models to generally characterize the expected trends relating viscous anisotropy to geodynamic processes. More quantitative characterization of the impact of viscous anisotropy will require more sophisticated modeling efforts.

## 5.1 Change in the direction of plate motion

636

637 By changing the orientation of the shear force in the horizontal direction (e.g. *Fig. 5A*), we
638 demonstrate that the asthenospheric texture should significantly influence the motion of a
639 tectonic plate. Indeed, for horizontally-oriented shear, the effective viscosity of an olivine
640 aggregate may be a factor of ~5 times smaller when the shear force is parallel to the mean
641 orientation of the a-axis of olivine grains (*ori-a*) compared to perpendicular to *ori-a* (*Fig. 10*).
642 Thus, if the texture beneath the plate is characterized by strong alignment of the a-axes, then a
643 large change in the orientation of forces on the plate may result in a significant slowing of the
644 plate velocity (up to a factor of 5 in the case of a uniformly-deforming asthenosphere), even if
645 the change in the orientation of forces occurs over a period of more than 10 million years
646 (*Fig. 6*). The stronger the initial texture (e.g., formed as a result of strains greater than 2, *Fig.
647 7*), and the larger the change in the orientation of the plate driving force (e.g., more than 45°,
648 *Fig. 8*), the larger and more lasting the asthenospheric resistance will be to changes in the
649 orientation of the driving forces. This asthenospheric resistance, induced by shear forces
650 misaligned with the preferred orientation of the texture, can also result in plate motion that is
651 not parallel to the plate driving force (*Figs. 6A, 7A, 8A*). This misalignment can last for 10s of
652 millions of years because the asthenospheric texture may be slow to redevelop.

653 Thus, we expect that anisotropic viscosity may significantly modify the relationship between
654 plate motions and the forces that drive them (e.g., Becker et al., 2006; Conrad and Lithgow-
655 Bertelloni, 2004). Although Becker and Kawakatsu (2011) found that mantle flow models that
656 included viscosity anisotropy behaved similarly to isotropic models, their study did not
657 examine time-dependent behavior. Instead, our results suggest that time-dependent changes to
658 the driving forces on plates, or to the amplitude or orientation of the anisotropic texture
659 beneath them, should result in potentially large differences between the orientation of the net
660 driving force on a plate and the direction of the resulting asthenospheric flow and plate
661 motion. Note that the effective viscosity of the asthenosphere may also vary spatially beneath
662 the plate depending on the orientation and maturity of the olivine texture locally. These
663 spatial, temporal, and directional differences in the resistance that the asthenosphere exerts on
664 plate motions may persist for durations of 10s of Myr (e.g., *Fig. 8*).

665 Our results suggest that anisotropic viscosity may cause a plate to respond only sluggishly to
666 changes in the direction of its driving forces. Indeed, plate motions in global plate
667 reconstruction models are observed to remain relatively stable for long periods (10s of Myr),
668 except for a few brief periods of global reorganization (Bercovici et al., 2000). This overall

669    stability has been attributed to slow evolution of the plate driving forces (e.g., Richards and

670    Lithgow-Bertelloni, 1996), despite the possibility that slab breakoff (Andrews and Billen,

671    2009) or even a change in the direction and magnitude of subduction-related stresses (e.g.,

672    Capitanio et al., 2011; Jahren et al., 2005) may change the driving forces on plates quickly.

673    The sluggishness with which anisotropic textures adjust to changes in the orientation of the

674    applied driving force may represent an alternative mechanism to explain the gradual changes

675    in the direction of plate motions observed in reconstructions. This mechanism predicts that

676    driving forces, asthenospheric resistance, and hence plate motions may be misaligned for

677    significant periods of time. Indeed such misalignment might be relevant for the Pacific plate

678    over the past 20 Myr (Faccenna et al., 2012).

679    ### 5.2 Transform faults

680    Asthenospheric mantle, sheared by plate motions, should experience shear stresses in a

681    horizontal direction on vertical planes near transform faults. Strain that results from these

682    stresses will be enhanced by viscous anisotropy. If the shearing direction is parallel to the

683    plate motions that generated the asthenospheric texture ($F_4$ in *Fig. 4*; *Fig. 5C; Fig. 10*) the

684    initially weakened asthenosphere will likely become stronger due to the evolving texture that

685    results in a strengthening, girdle-like distribution. For transform motion perpendicular to this

686    texture ($F_6$ in *Fig. 4*; *Fig. 5C; Fig. 10*), the initial rotation of the olivine grains significantly

687    weakens the asthenosphere. Interestingly, the results of this simple analysis are consistent

688    with the large number of transform faults in the oceanic lithosphere. Although transform

689    faults usually form close to the ridge where the asthenosphere has not been sheared for long,

690    and where texture development involves a more complicated history associated with corner

691    flow (Blackman et al., 2017), it is possible that the low asthenospheric resistance aids the

692    formation of lithospheric scale transform faults.

693    ### 5.3 Initiation of subduction or dripping

694    Changing the direction of the shear force from horizontal to vertical can be roughly associated

695    with the initiation of slab subduction or dripping of lithospheric mantle. Our results ($F_3$ and $F_5$

696    in *Fig. 5A&B, Fig. 10*) suggest that asthenosphere with well-oriented olivine grains imposes

697    small resistance for such processes if they are oriented perpendicular to the initial plate-

698    motion direction, but large resistance if they are oriented on the plane that is parallel to the

699    plate motion. This finding is consistent with the observed orientation of subduction trenches,

700    which are usually close to perpendicular to the long-term plate motion direction. Motion in

response to a vertically-oriented shear force on a plane perpendicular to the initial plate-motion direction (e.g, trench-perpendicular subduction, $F_3$ in *Figure 4*) exhibits a short period of increased resistance to deformation that must be overcome before the texture weakens (*Figure 5C,* blue curve). Thus, asthenospheric textures may initially pose a slight impediment to subduction initiation, but after a few Myrs, the olivine texture evolution may hasten the evolution of subduction. In contrast, vertical motion in response to a vertical shear force on a plane parallel to plate motions (e.g., very oblique subduction or Richter-rolls, $F_1$ to $F_5$ in *Fig. 4*) is highly resisted by the anisotropic fabric, but in the long term, olivine texture development induces asthenospheric weakening, which may allow for accelerated growth of lithospheric instabilities (*Fig. 5B*, orange curve).

However, both subduction initiation and small-scale convection involve more complex deformation than the simple instantaneous change in shear direction that is modeled here. For example, subduction zones often start along transform faults or in the vicinity of active subductions (Crameri et al., 2020), both of which can fundamentally change the asthenospheric texture and hence its resistance to the formation of new slabs or lithospheric instabilities. The rheology of the lithosphere also plays a potentially large role in subduction initiation, and it is possible that olivine texture can become frozen into the oceanic lithosphere as it cools (Tommasi, 1998), which would likely affect the rheology of the plate, and hence, its resistance to bending. Although analysis of this deformation is beyond the scope of this study, the combined effect of asthenospheric and lithospheric weakening due to anisotropy could allow for subduction zone initiation in response to lower tectonic stresses than usually expected (e.g., Gurnis et al., 2004). To explore the role of asthenospheric and lithospheric viscous anisotropy in such complex processes, more sophisticated 3D geodynamic modeling is required.


## 6. *Conclusions*

Olivine texture development in the asthenosphere and its response to shearing are highly coupled and can exert considerable influences on geodynamic processes. In response to unidirectional shearing of the asthenosphere, the formation of an olivine texture causes a significant decrease in effective mantle viscosity after accumulating a shear strain of ~5. After this texture has formed, changes to the direction of the forces on the system, as induced by a change in the tectonic setting, result in a different effective viscosity because of the

mechanically anisotropic nature of the textured asthenosphere. Our results indicate that differences in the effective viscosity associated with shearing asthenosphere primarily result from the relative activation of olivine's weak and strong slip systems. The resulting differences in effective viscosity can be over an order of magnitude, and should hinder some tectonic processes and foster others, depending on their sense of deformation relative to asthenospheric textures (*Fig. 10*). If the new shear direction is such that the strongest slip system, (010)[001], has to be activated to produce deformation, then the effective viscosity will increase. This increase is generally the case for a change in the direction of plate motion or vertical shearing on a plane parallel to plate motions. In contrast, the mantle should remain weak, or even become weaker, for shear forces that primarily induce deformation on the other two, weaker slip systems, (010)[100] and (001)[100], which is the case for transform motions, subduction initiation, or ongoing plate motion in the same direction. Thus, based on our simple models, we expect asthenospheric textures to significantly slow changes to the direction of plate motions and hinder the formation of ridge-perpendicular subduction zones. Conversely, these textures should assist in the initiation of new subduction zones parallel to mid-ocean ridges (perpendicular to plate motion) and promote the development of lithospheric scale transform faults. To fully understand the impact of anisotropic viscosity on plate tectonics and asthenospheric dynamics, olivine texture development, and the anisotropic viscosity that is associated with it, needs to be integrated into 3D dynamic models of the relevant processes.

## Acknowledgement

## References

Andrews, E.R., Billen, M.I., 2009. Rheologic controls on the dynamics of slab detachment. Tectonophysics, Interpreting the tectonic evolution of Pacific Rim margins using plate

763 kinematics and slab window volcanism 464, 60–69.

764 https://doi.org/10.1016/j.tecto.2007.09.004

765 Bamford, D., Crampin, S., 1977. Seismic anisotropy - the state of the art. Geophysical Journal

766 Of The Royal Astronomical Society 49, 1–8. https://doi.org/10.1111/j.1365-

767 246X.1977.tb03697.x

768 Becker, T.W., 2008. Azimuthal seismic anisotropy constrains net rotation of the lithosphere.

769 Geophys. Res. Lett. 35, L05303. https://doi.org/10.1029/2007GL032928

770 Becker, T.W., Chevrot, S., Schulte-Pelkum, V., Blackman, D.K., 2006. Statistical properties

771 of seismic anisotropy predicted by upper mantle geodynamic models. Journal of

772 Geophysical Research: Solid Earth 111. https://doi.org/10.1029/2005JB004095

773 Becker, T.W., Conrad, C.P., Schaeffer, A.J., Lebedev, S., 2014. Origin of azimuthal seismic

774 anisotropy in oceanic plates and mantle. Earth and Planetary Science Letters 401, 236–250.

775 https://doi.org/10.1016/j.epsl.2014.06.014

776 Becker, T.W., Kawakatsu, H., 2011. On the role of anisotropic viscosity for plate-scale flow.

777 Geophysical Research Letters 38, 1–5. https://doi.org/10.1029/2011GL048584

778 Becker, T.W., Kellogg, J.B., Ekström, G., O'Connell, R.J., 2003. Comparison of azimuthal

779 seismic anisotropy from surface waves and finite strain from global mantle-circulation

780 models. Geophys J Int 155, 696–714. https://doi.org/10.1046/j.1365-246X.2003.02085.x

781 Becker, T.W., Kustowski, B., Ekström, G., 2008. Radial seismic anisotropy as a constraint for

782 upper mantle rheology. Earth and Planetary Science Letters 267, 213–227.

783 https://doi.org/10.1016/j.epsl.2007.11.038

784 Beghein, C., Yuan, K., Schmerr, N., Xing, Z., 2014. Changes in Seismic Anisotropy Shed

785 Light on the Nature of the Gutenberg Discontinuity. Science 343, 1237–1240.

786 https://doi.org/10.1126/science.1246724

787 Behn, M.D., Conrad, C.P., Silver, P.G., 2004. Detection of upper mantle flow associated with

788 the African Superplume. Earth and Planetary Science Letters 224, 259–274.

789 https://doi.org/10.1016/j.epsl.2004.05.026

790 Bercovici, D., Ricard, Y., Richards, M.A., 2000. The Relation between mantle dynamics and

791 plate tectonics: A Primer, in: Richards, M.A., Gordon, R.G., van der Hilst, R.D. (Eds.),

792 Geophysical Monograph Series. American Geophysical Union, Washington, D. C., pp. 5–

793 46. https://doi.org/10.1029/GM121p0005

794    Blackman, D.K., Boyce, D.E., Castelnau, O., Dawson, P.R., Laske, G., 2017. Effects of
795       crystal preferred orientation on upper-mantle flow near plate boundaries: rheologic
796       feedbacks and seismic anisotropy. Geophysical Journal International 210, 1481–1493.
797       https://doi.org/10.1093/gji/ggx251

798    Boneh, Y., Morales, L.F.G., Kaminski, E., Skemer, P., 2015. Modeling olivine CPO evolution
799       with complex deformation histories: Implications for the interpretation of seismic anisotropy
800       in the mantle. Geochemistry, Geophysics, Geosystems 16, 3436–3455.
801       https://doi.org/10.1002/2015GC005964

802    Bunge, H., 1982. Texture Analysis in Materials Science: Mathematical Models. Butterworths,
803       London.

804    Capitanio, F.A., Faccenna, C., Zlotnik, S., Stegman, D.R., 2011. Subduction dynamics and
805       the origin of Andean orogeny and the Bolivian orocline. Nature 480.

806    Christensen, N.I., 1984. The magnitude, symmetry and origin of upper mantle anisotropy
807       based on fabric analyses of ultramafic tectonites. Geophysical Journal International 76, 89–
808       111. https://doi.org/10.1111/j.1365-246X.1984.tb05025.x

809    Christensen, U.R., 1987. Some geodynamical effects of anisotropic viscosity. Geophysical
810       Journal of the Royal Astronomical Society 91, 711–736. https://doi.org/10.1111/j.1365-
811       246X.1987.tb01666.x

812    Conrad, C.P., Behn, M.D., 2010. Constraints on lithosphere net rotation and asthenospheric
813       viscosity from global mantle flow models and seismic anisotropy: ANISOTROPY AND
814       LITHOSPHERE NET ROTATION. Geochem. Geophys. Geosyst. 11, n/a-n/a.
815       https://doi.org/10.1029/2009GC002970

816    Conrad, C.P., Lithgow-Bertelloni, C., 2004. The temporal evolution of plate driving forces:
817       Importance of "slab suction" versus "slab pull" during the Cenozoic. Journal of Geophysical
818       Research B: Solid Earth 109, 1–14. https://doi.org/10.1029/2004JB002991

819    Crameri, F., Magni, V., Domeier, M., Shephard, G.E., Chotalia, K., Cooper, G., Eakin, C.M.,
820       Grima, A.G., Gürer, D., Király, Á., Mulyukova, E., Peters, K., Robert, B., Thielmann, M.,
821       2020. A transdisciplinary and community-driven database to unravel subduction zone
822       initiation. Nature Communications 11, 3750. https://doi.org/10.1038/s41467-020-17522-9

823 Dellinger, J., Vasicek, D., Sondergeld, C., 1998. Kelvin Notation for Stabilizing Elastic-
824     Constant Inversion. Revue de l'Institut Français du Pétrole 53, 709–719.
825     https://doi.org/10.2516/ogst:1998063

826 Durham, W.B., Goetze, C., 1977. Plastic flow of oriented single crystals of Olivine 1.
827     Mechanical Data. Journal of Geophysical Research 82, 5737–5753.

828 Eakin, C.M., Rychert, C.A., Harmon, N., 2018. The Role of Oceanic Transform Faults in
829     Seafloor Spreading: A Global Perspective From Seismic Anisotropy. Journal of Geophysical
830     Research: Solid Earth 123, 1736–1751. https://doi.org/10.1002/2017JB015176

831 Faccenna, C., Becker, T.W., Lallemand, S., Steinberger, B., 2012. On the role of slab pull in
832     the Cenozoic motion of the Pacific plate. Geophysical Research Letters 39, 1–6.
833     https://doi.org/10.1029/2011GL050155

834 Gaboret, C., Forte, A.M., Montagner, J.-P., 2003. The unique dynamics of the Pacific
835     Hemisphere mantle and its signature on seismic anisotropy. Earth and Planetary Science
836     Letters 208, 219–233. https://doi.org/10.1016/S0012-821X(03)00037-2

837 Gerya, T.V., 2016. Origin, Evolution, Seismicity, and Models of Oceanic and Continental
838     Transform Boundaries, in: Plate Boundaries and Natural Hazards. American Geophysical
839     Union (AGU), pp. 39–76. https://doi.org/10.1002/9781119054146.ch3

840 Gurnis, M., Hall, C., Lavier, L., 2004. Evolving force balance during incipient subduction.
841     Geochemistry, Geophysics, Geosystems 5. https://doi.org/10.1029/2003GC000681

842 Hansen, L.N., Conrad, C.P., Boneh, Y., Skemer, P., Warren, J.M., Kohlstedt, D.L., 2016a.
843     Viscous anisotropy of textured olivine aggregates: 2. Micromechanical model. Journal of
844     Geophysical Research: Solid Earth 121, 7137–7160. https://doi.org/10.1002/2016JB013304

845 Hansen, L.N., Warren, J.M., Zimmerman, M.E., Kohlstedt, D.L., 2016b. Viscous anisotropy
846     of textured olivine aggregates, Part 1: Measurement of the magnitude and evolution of
847     anisotropy. Earth and Planetary Science Letters 445, 92–103.
848     https://doi.org/10.1016/j.epsl.2016.04.008

849 Hansen, L.N., Zimmerman, M.E., Kohlstedt, D.L., 2012. Laboratory measurements of the
850     viscous anisotropy of olivine aggregates. Nature 492, 415–418.
851     https://doi.org/10.1038/nature11671

852    Jahren, A.H., Conrad, C.P., Arens, N.C., Mora, G., Lithgow-Bertelloni, C., 2005. A plate
853    tectonic mechanism for methane hydrate release along subduction zones. Earth and Planetary
854    Science Letters 236, 691–704. https://doi.org/10.1016/j.epsl.2005.06.009

855    Kaminski, É., Ribe, N.M., 2002. Timescales for the evolution of seismic anisotropy in mantle
856    flow. Geochemistry, Geophysics, Geosystems 3, 1–17.
857    https://doi.org/10.1029/2001GC000222

858    Karato, S., 1987. Seismic anisotropy due to lattice preferred orientation of minerals:
859    Kinematic or dynamic?, in: Manghnani, M.H., Syono, Y. (Eds.), Geophysical Monograph
860    Series. American Geophysical Union, Washington, D. C., pp. 455–471.
861    https://doi.org/10.1029/GM039p0455

862    Karato, S., Wu, P., 1993. Rheology of the Upper Mantle: A Synthesis. Science 260, 771–778.

863    Lev, E., Hager, B.H., 2011. Anisotropic viscosity changes subduction zone thermal structure.
864    Geochemistry, Geophysics, Geosystems 12. https://doi.org/10.1029/2010GC003382

865    Lev, E., Hager, B.H., 2008. Rayleigh-Taylor instabilities with anisotropic lithospheric
866    viscosity. Geophysical Journal International 173, 806–814. https://doi.org/10.1111/j.1365-
867    246X.2008.03731.x

868    Long, M.D., 2013. Constraints on Subduction Geodynamics From Seismic Anisotropy.
869    Reviews of Geophysics 51, 76–112. https://doi.org/10.1002/rog.20008

870    Long, M.D., Becker, T.W., 2010. Mantle dynamics and seismic anisotropy. Earth and
871    Planetary Science Letters 297, 341–354. https://doi.org/10.1016/j.epsl.2010.06.036

872    Mainprice, D., Bachmann, F., Hielscher, R., Schaeben, H., 2015. Descriptive tools for the
873    analysis of texture projects with large datasets using MTEX : strength, symmetry and
874    components. Geological Society, London, Special Publications 409, 251–271.
875    https://doi.org/10.1144/SP409.8

876    Mühlhaus, H.-B., Čada, M., Moresi, L., 2003. Anisotropic Convection Model for the Earth's
877    Mantle, in: Sloot, P.M.A., Abramson, D., Bogdanov, A.V., Gorbachev, Y.E., Dongarra, J.J.,
878    Zomaya, A.Y. (Eds.), Computational Science — ICCS 2003. Springer Berlin Heidelberg,
879    Berlin, Heidelberg, pp. 788–797. https://doi.org/10.1007/3-540-44863-2_77

880    Mühlhaus, H.-B., Moresi, L., Hobbs, B., Dufour, F., 2002. Large Amplitude Folding in Finely
881    Layered Viscoelastic Rock Structures. Pure and Applied Geophysics 159, 2311–2333.
882    https://doi.org/10.1007/s00024-002-8737-4

883 Pouilloux, L., Kaminski, E., Labrosse, S., 2007. Anisotropic rheology of a cubic medium and
884 implications for geological materials. Geophysical Journal International 170, 876–885.
885 https://doi.org/10.1111/j.1365-246X.2007.03461.x

886 Richards, M.A., Lithgow-Bertelloni, C., 1996. Plate motion changes, the Hawaiian-Emperor
887 bend, and the apparent success and failure of geodynamic models. Earth and Planetary
888 Science Letters 137, 19–27. https://doi.org/10.1016/0012-821X(95)00209-U

889 Schellart, W.P., 2004. Kinematics of subduction and subduction-induced flow in the upper
890 mantle. Journal of Geophysical Research B: Solid Earth 109, 1–19.
891 https://doi.org/10.1029/2004JB002970

892 Signorelli, J., Tommasi, A., 2015. Modeling the effect of subgrain rotation recrystallization
893 on the evolution of olivine crystal preferred orientations in simple shear. Earth and Planetary
894 Science Letters 430, 356–366. https://doi.org/10.1016/j.epsl.2015.08.018

895 Silver, P.G., 1996. SEISMIC ANISOTROPY BENEATH THE CONTINENTS: Probing the
896 Depths of Geology. Annu. Rev. Earth Planet. Sci. 24, 385–432.
897 https://doi.org/10.1146/annurev.earth.24.1.385

898 Skemer, P., Katayama, I., Jiang, Z., Karato, S., 2005. The misorientation index: Development
899 of a new method for calculating the strength of lattice-preferred orientation. Tectonophysics
900 411, 157–167. https://doi.org/10.1016/j.tecto.2005.08.023

901 Stixrude, L., Lithgow-Bertelloni, C., 2005. Mineralogy and elasticity of the oceanic upper
902 mantle: Origin of the low-velocity zone. Journal of Geophysical Research: Solid Earth (1978–
903 2012) 110. https://doi.org/10.1029/2004JB002965

904 Tanimoto, T., Anderson, D.L., 1984. Mapping convection in the mantle. Geophysical
905 Research Letters 11, 287–290. https://doi.org/10.1029/GL011i004p00287

906 Taylor, G.I., 1938. Plastic Strain in Metals. Journal of Inst. Met. 62.

907 Tommasi, A., 1998. Forward modeling of the development of seismic anisotropy in the upper
908 mantle. Earth and Planetary Science Letters 160, 1–13. https://doi.org/10.1016/S0012-
909 821X(98)00081-8

910 Vollmer, F.W., 1990. An application of eigenvalue methods to structural domain analysis.
911 Bulletin of the Geological Society of America 102, 786–791. https://doi.org/10.1130/0016-
912 7606(1990)102<0786:AAOEMT>2.3.CO;2

913   Yuan, H., Romanowicz, B., 2010. Lithospheric layering in the North American craton. Nature

914   466, 1063–1068. https://doi.org/10.1038/nature09332
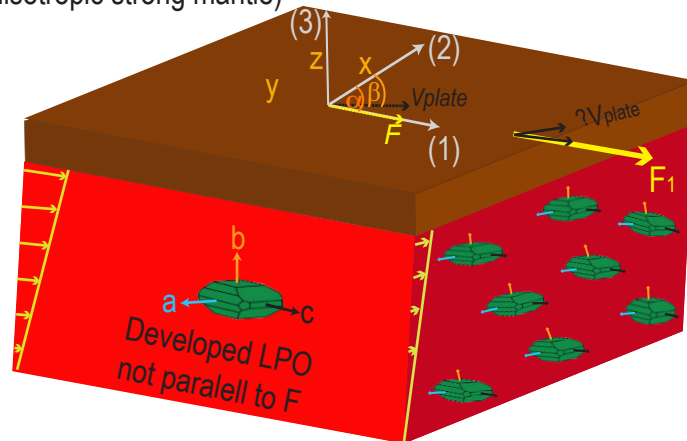
915

**Figures**

A) Shear force applied to isotropic mantle
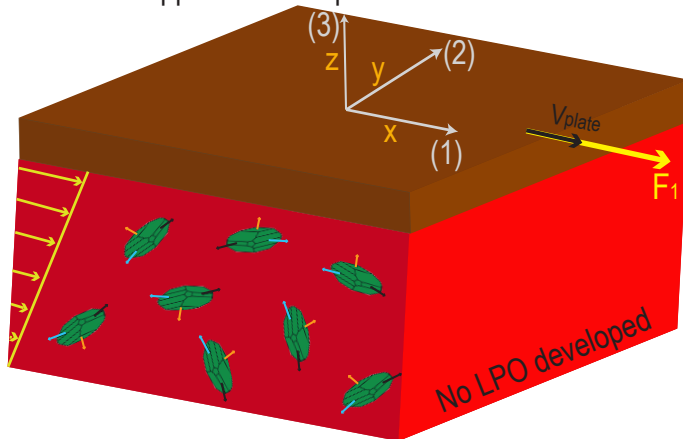


B) Shear force applied parallel to developed LPO
(anisotropic weak mantle)
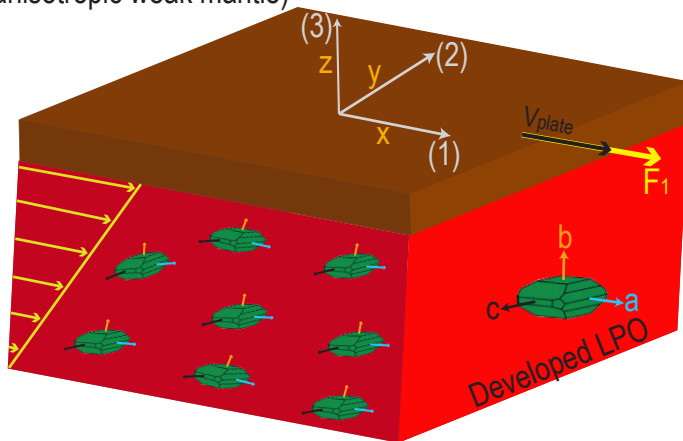
C) Shear force applied perpendicular to LPO
(anisotropic strong mantle)

917

*Figure 1: Relationship between anisotropic viscosity and olivine texture formation. A) A force*
*($F_1$) applied to an initially isotropic asthenosphere (i.e., without a pre-existing texture) yields*
*a moderate plate speed, and the associated asthenospheric deformation fosters olivine texture*
*development. B) The same force applied parallel to the a-axis of a well-developed texture*
*results in a much larger plate speed. C) Applying this force parallel to the c-axis causes the*

*plate to move much more slowly. The configuration depicted in panel (B) can evolve into the*
*configuration depicted in panel (C) in two ways. Either the force can be rotated relative to the*
*texture (as for many geodynamic scenarios) or the texture can be rotated with respect to the*
*force (as illustrated in (C) and implemented in our modeling effort).*
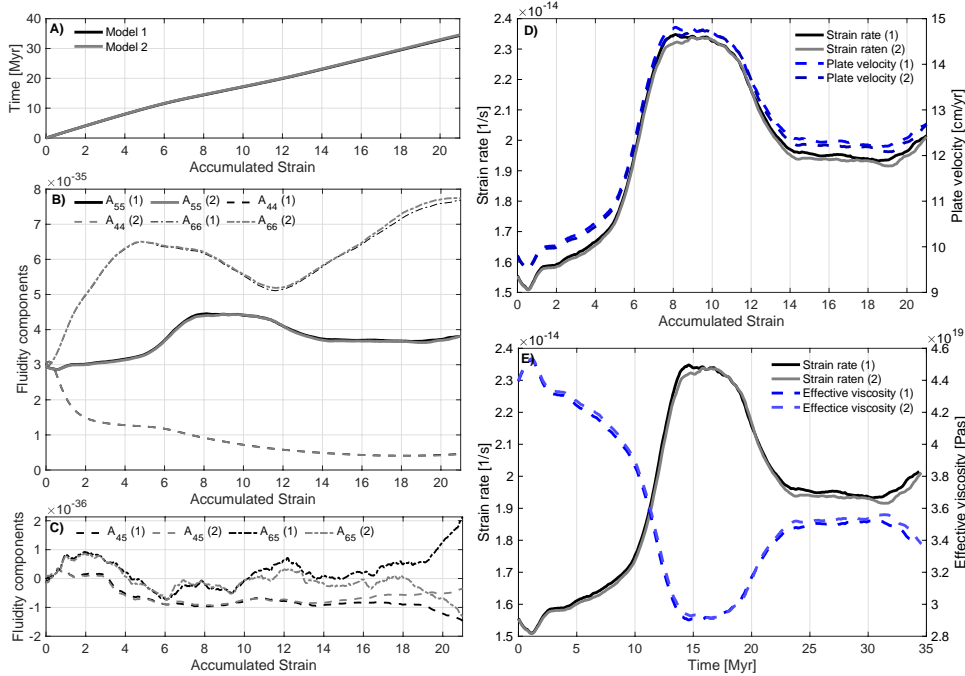


*Figure 2: Results of two sets of models with constant shear stress ($\sigma_{13}$= 0.68 MPa), both*
*computed as average results from 5 model runs each starting from 1000 uniformly distributed*
*grain orientations. A) Accumulated strain as a function of time. B) Shear components of the*
*fluidity parameter tensor. $A_{44}$ and $A_{66}$ are fictive curves since the associated stresses for these*
*components, $\sigma_{23}$ and $\sigma_{12}$, are zero. $A_{55}$ represents the fluidity for the actual applied stress $\sigma_{13}$.*
*C) Fluidity components relating strain rates in the perpendicular direction ($A_{45}$) or plane*
*($A_{65}$) with respect to the shear stress ($\sigma_{13}$). D) Strain rate ($|\dot{\varepsilon}|$) and plate velocity ($v_{plate}$) as a*
*function of the accumulated strain. The plate velocity is calculated from the horizontal strain*
*rate component (eq. 10), while the strain-rate curve is the norm of the shear strain rate tensor*
*(for which only the non-diagonal components are non-zero). E) Strain rate and effective*
*viscosity as a function of time instead of accumulated strain.*
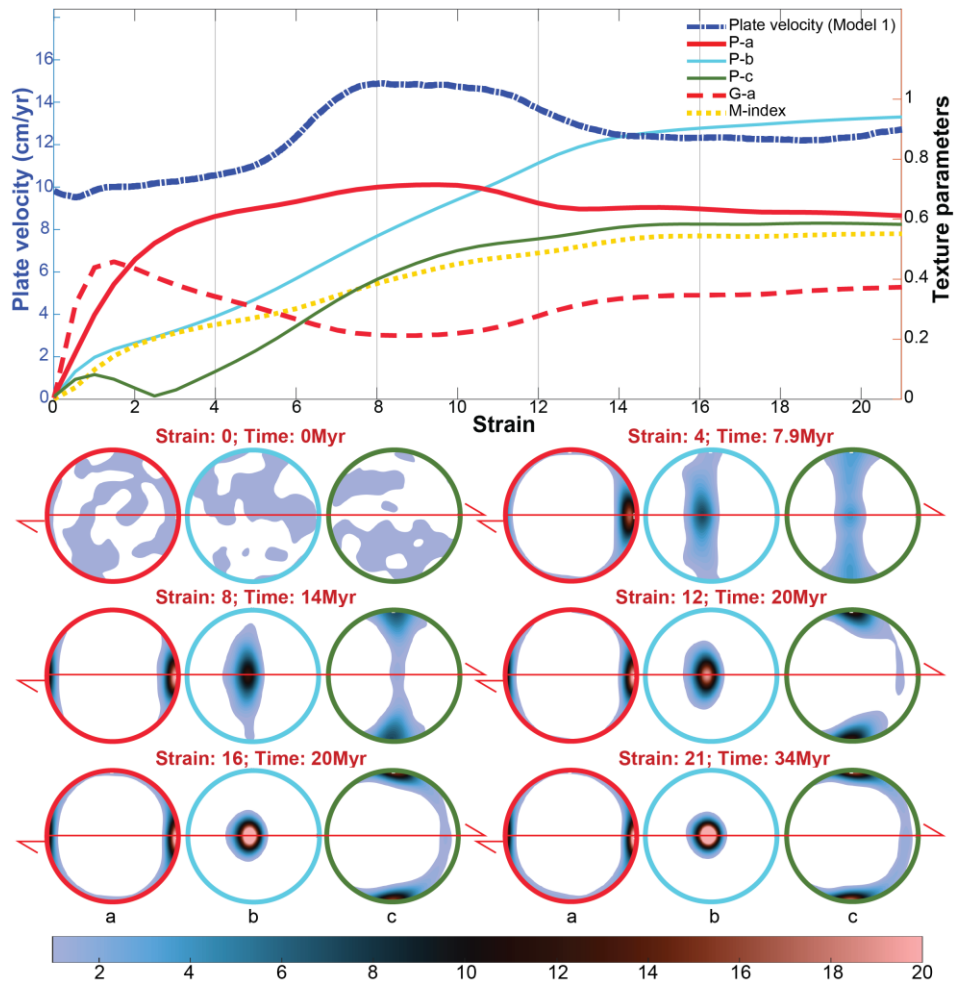
940

*Figure 3: The evolution of plate velocity and several texture parameters as a function of accumulated strain (top panel) with pole figures (below) indicating the orientation density of a-, b-, and c- axes for olivine aggregates with different total strains. The color scale indicates multiples of a uniform density. The shear direction (marked by red arrows) is towards the right and the shear plane is the same as the figure's plane.*

941
942
943
944
945

946

Possibilities for changing the shear force

947
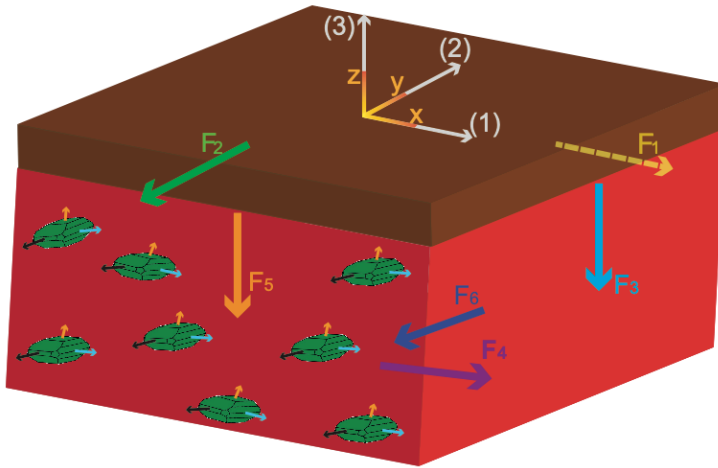
948 *Figure 4: Possible orientations for the shear force, with $F_1$ representing the orientation*
949 *associated with initial plate motion (e.g., as in Fig. 1b). $F_2$ represents a shear force acting on*
950 *a horizonal plane at 90° to the initial plate motion direction, analogous to a change in the*
951 *direction of the plate driving force. $F_4$ and $F_6$ represent forces that create shearing*
952 *deformation in a horizontal direction along vertical planes, analogous to transform shear*
953 *zones. $F_3$ and $F_5$ represent forces that create shearing deformation in a vertical direction on*
954 *vertical planes, analogous to subduction initiation or a dripping instability. In our analysis,*
955 *all forces have the same magnitude as $F_1$.*

956

957



958
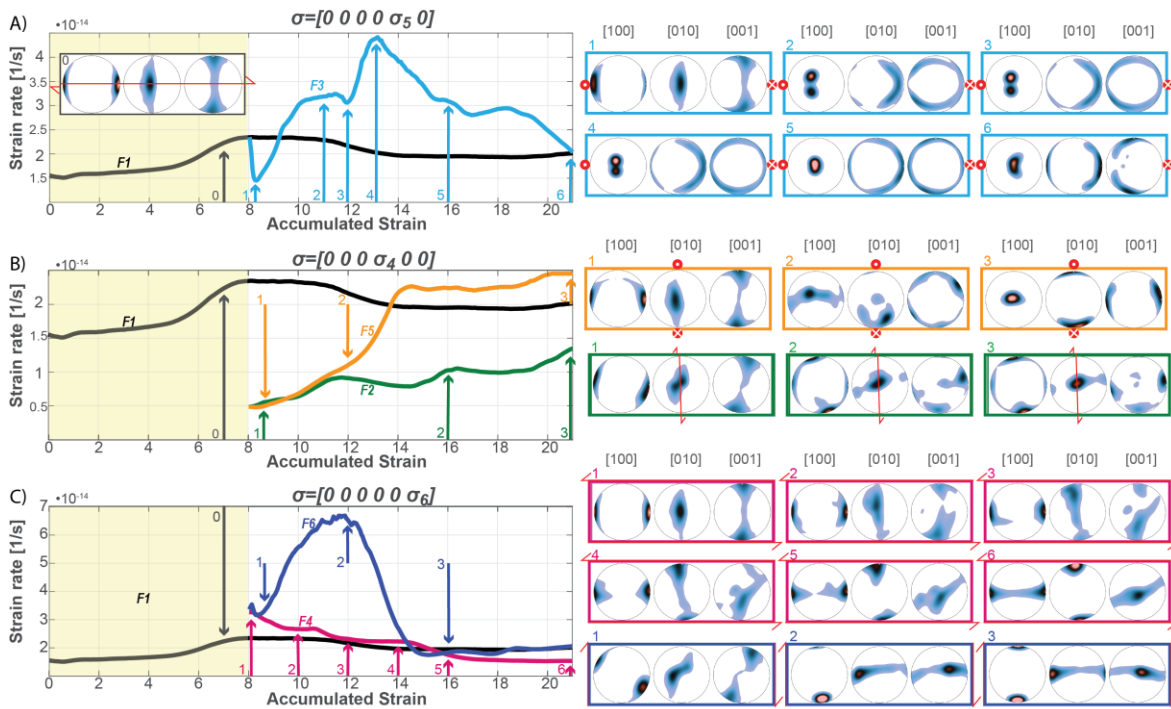
959 *Figure 5: Strain rate as a function of accumulated strain for the five different changes to the*
960 *imposed shear force (Fig. 4). On the left side, an initially isotropic aggregate is deformed*

*with shear force $F_1$ until a strain of 8 (as in Fig. 2D). At a strain of 8, the direction of the shear force is instantaneously changed to the directions $F_2$ through $F_6$ (Fig. 4). Plots are grouped based on reciprocal pairs of deformation responding to the same imposed stress (see text). On the right side, pole figures indicate the texture for several points in the evolution denoted by arrows in the left diagrams. Note that all of the textures are presented relative to the mantle reference frame, and the shear force acting on the mantle is marked by red arrows (and arrow points and tails).*
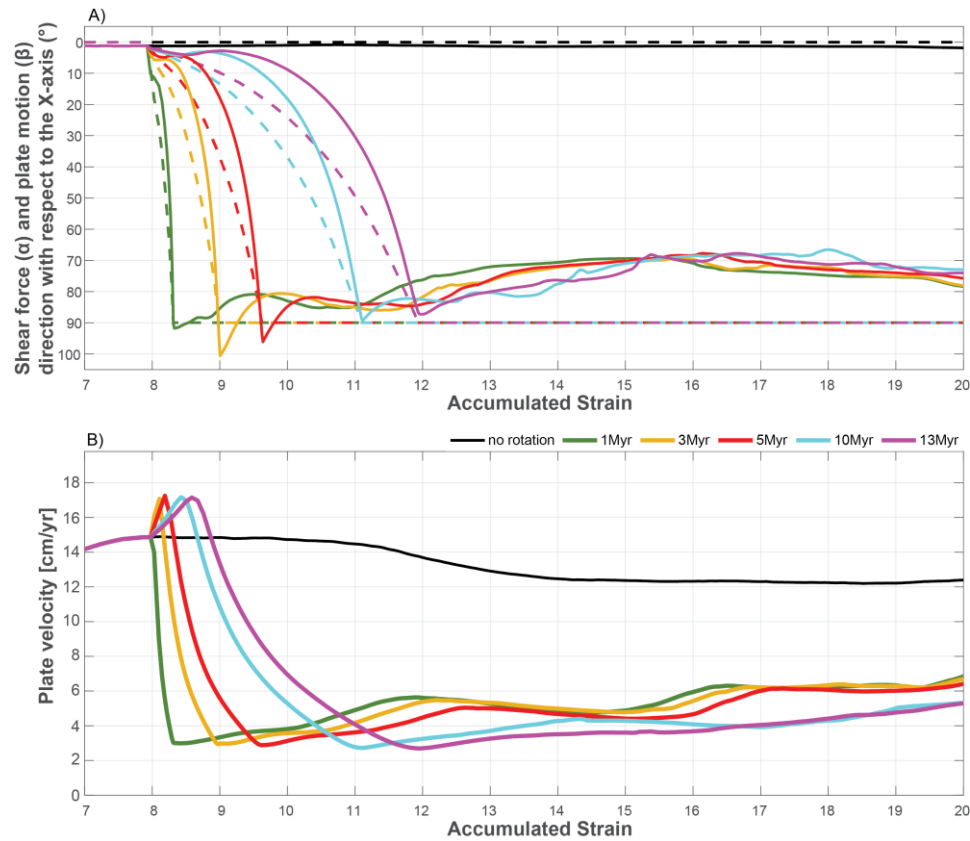


*Figure 6: Results from models with different rates of imposed rotation of the shear stress. An initial texture (associated with an accumulated strain of 8, using model 1 of Fig. 2) is rotated 90° around the z-axis (representing a change from $F_1$ to $F_2$) within a period between 1 and 13 Myr. a) Change in the direction of the shear force (α, dashed lines) and plate motion (β, solid lines) with respect to the x-axis (fixed to the mantle), as a function of accumulated strain. b) Amplitude of the plate velocity as a function of accumulated strain.*
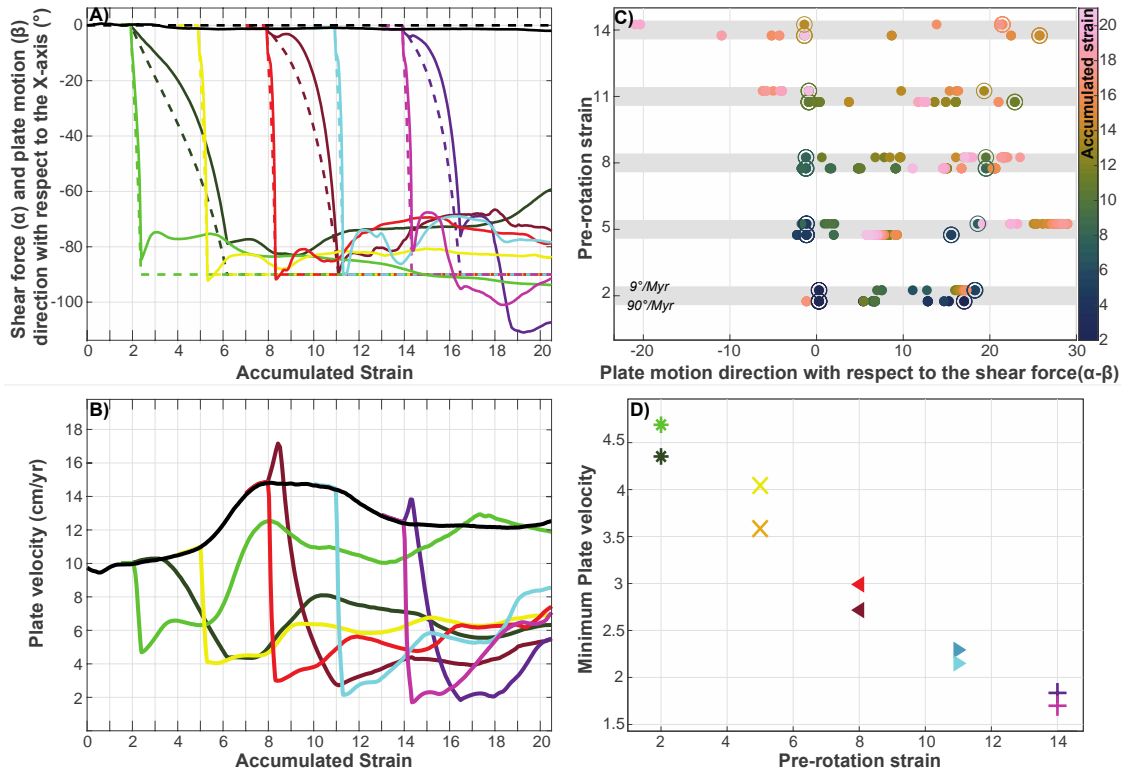
977

*Figure 7: Results from models with varying amounts of accumulated strain (and therefore texture strength) at the time of the rotation (Pre-rotation strain). A) Direction of the shear force (α, dashed lines) and the plate motion (β, solid lines) for models that rotate the texture 90° in either 1 Myr (lighter colors) or 10 Myr (darker colors). B) Corresponding plate velocity amplitudes vs. accumulated strain for the cases shown in (A). C) Local minimums and maximums of the plate-motion direction marked with dots that are color-coded according the accumulated strain (with respect to the shear force direction) for the five tested pre-rotation strains. For each switch strain, upper rows represent models using the 10 Myr rotation time while the lower rows use 1 Myr rotations. D) Minimum plate velocity (i.e., velocity right after the rotation) vs. the accumulated strain after which the rotation has happened.*
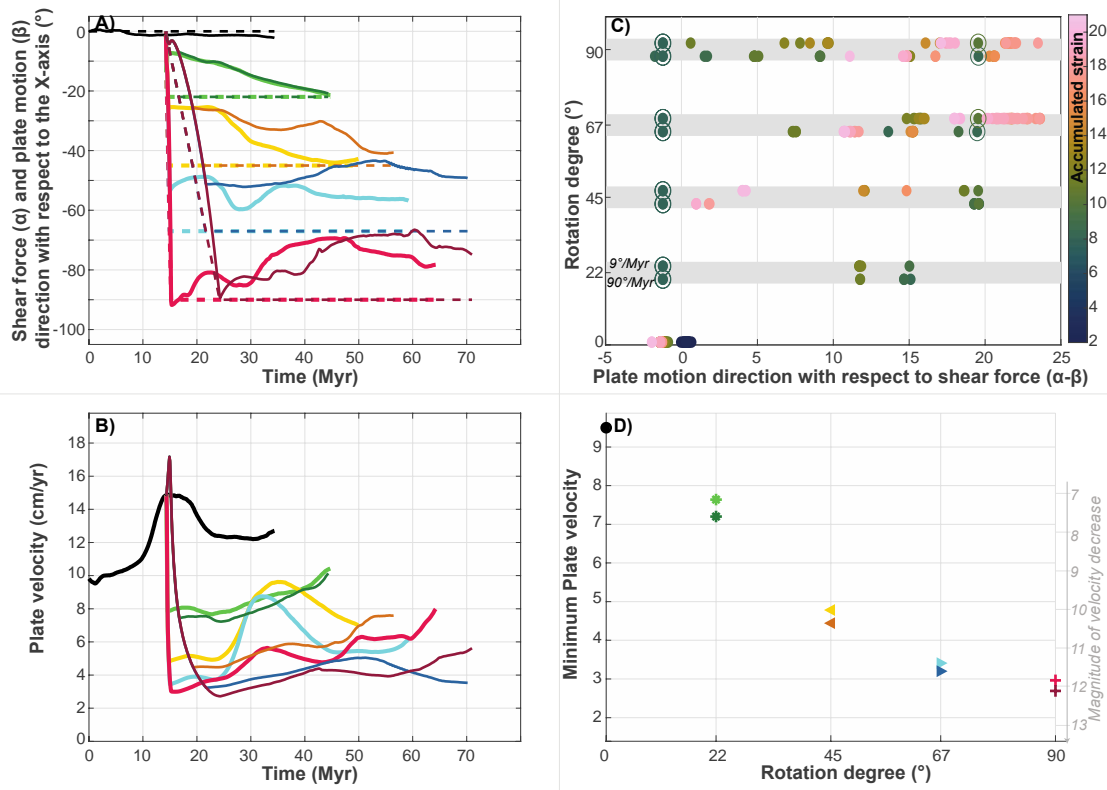
990

991 *Figure 8: Results from models with varying amounts of rotation around the z-axis. Panels are*
992 *the same as in Fig. 7, except using rotation angle instead of pre-rotation strain in (C) and*
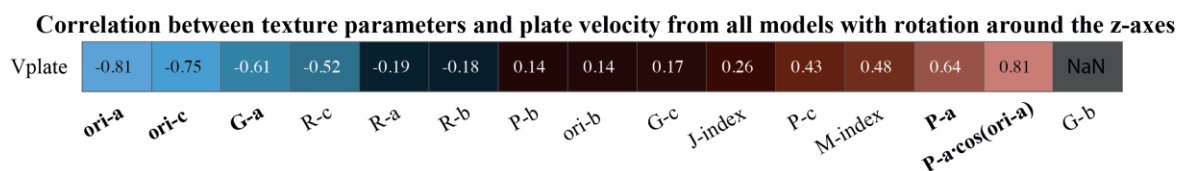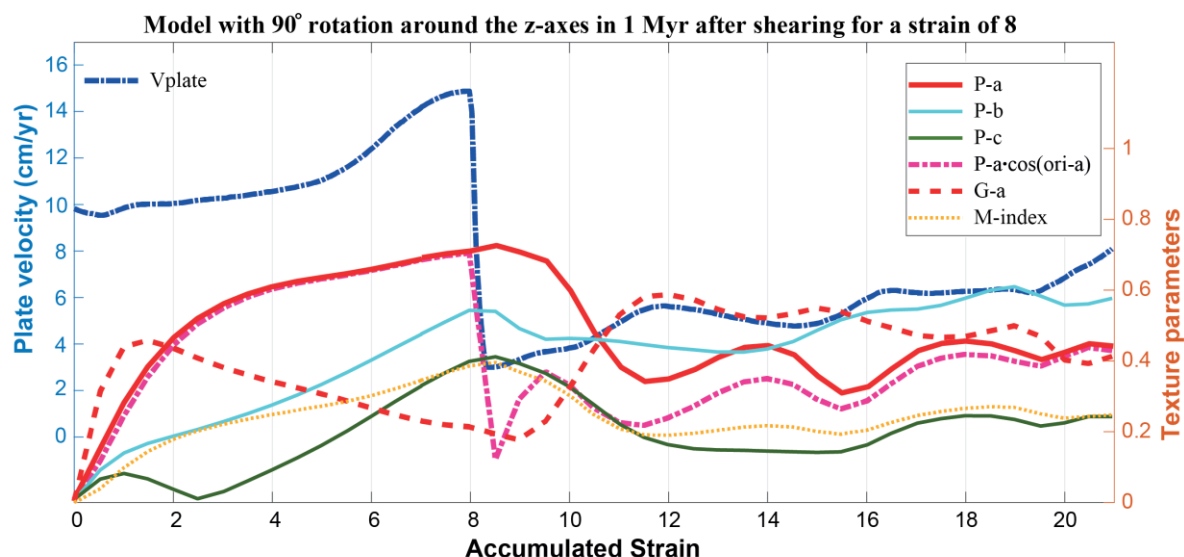993 *(D).*

994

995

*Figure 9: Top) plate velocity and texture parameters, as a function of accumulated strain, for a model in which a 90° rotation (representing a change from $F_1$ to $F_2$) is imposed over 1 Myr after a strain of 8 (the fastest rotation presented in Fig. 6). Bottom) correlation between texture parameters and plate velocity based on all models with rotation (0-90º) around the z-axis, listed in order from negative (blue shades) to positive (red shades) correlations. Abbreviations: $v_{plate}$ plate velocity; ori-a (-b; -c) mean orientation of the olivine a-axes (b-axes; c-axes); G, R, P (-a -b; -c) girdle, random, and point distribution parameters for each axes, respectively (Vollmer, 1990).*
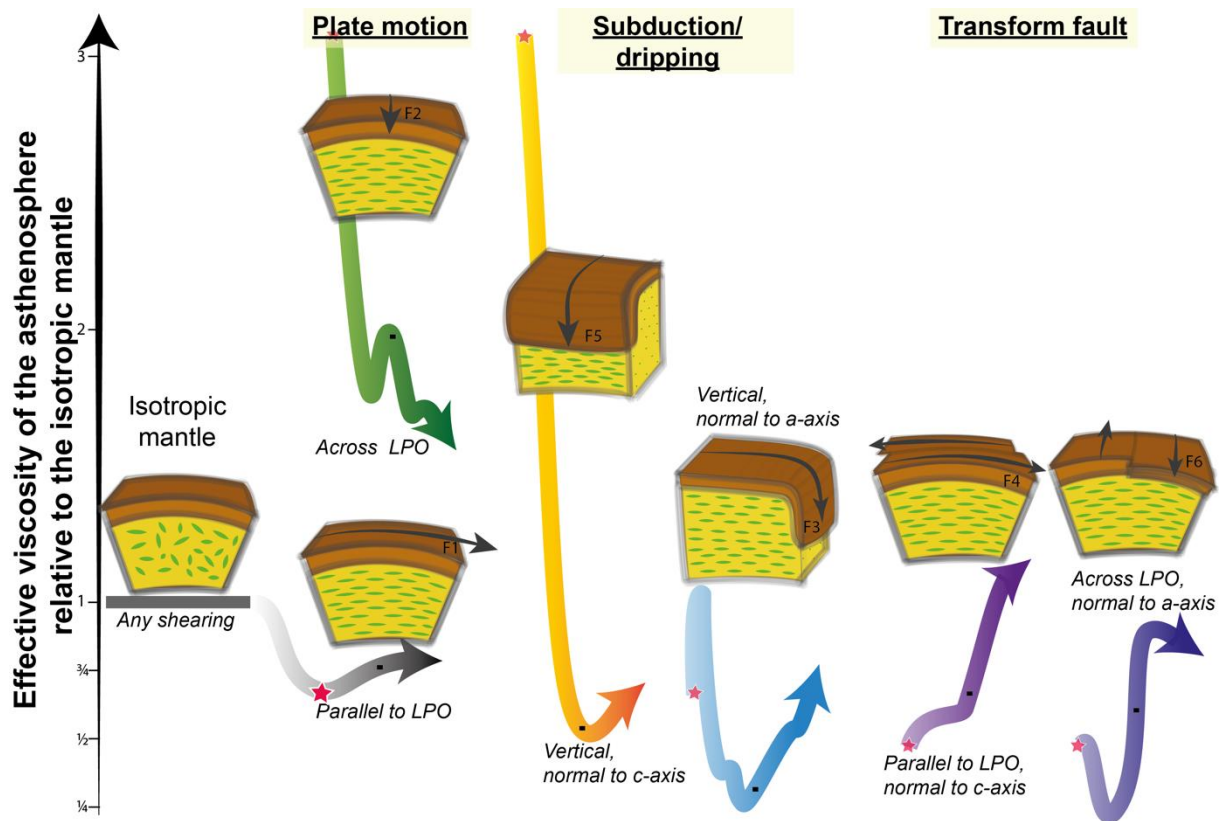
1004

*Figure 10: Trends for the manner in which anisotropic viscosity in the asthenosphere should influence different geodynamic situations. The white to black arrow indicates the mantle weakening path associated with development of an LPO as the asthenosphere accumulates strain due to simple shear (e.g. in model 1). The colored arrows indicate the time evolution of the relative effective viscosity (vertical dimension, values based on results shown in Fig. 5) from the moment of switching the shear direction (strain of 8, marked with a star) through an accumulated strain of 14 (post-rotation strain of 6, black squares), and until a strain of 21 (post-rotation strain of 13, indicated by the arrow tips). Geodynamic processes for which the effective viscosity increases ($F_2$ plate motion and $F_5$ subduction/dripping) could be initially impeded by anisotropic viscosity, while those for which the effective viscosity decreases ($F_3$ - subduction and dripping, and $F_4$ and $F_5$ - transform fault) could be initially promoted. Subsequent changes to the effective viscosity along each path indicate how continued texture development should either speed or slow each process as it develops.*